Characteristic of Weld Bead By Using Flat Wire Electrode In GMAW Inline During The Process: An Experimental And Numerical Analysis

K Sripriyan (ksp.mech@psgtech.ac.in)
PSG College of Technology
M Ramu
Amrita School of Engineering, Amirta Vishwa Vidyapeetham University
P R Thyla
PSG College of Technology
K Anantharuban
Tata Global Beverages Limited
M Karthigha
Sri Ramakrishna Engineering College

Research Article

Keywords: Arc welding, flat wire electrode, electromagnetic force, depth-to-width ratio, and temperature distribution

Posted Date: September 17th, 2021

DOI: https://doi.org/10.21203/rs.3.rs-847159/v1

Characteristic of weld bead by using flat wire electrode in GMAW inline during the Process: An Experimental and Numerical Analysis

Sripriyan K[1*] Ramu M[2] Thyla P R[1] Anantharuban K[3] Karthigha M[4]

[1] *Department of Mechanical Engineering, PSG College of Technology, Coimbatore, 641 004, India*
[2]*Department of Mechanical Engineering, Amrita School of Engineering, Amirta Vishwa Vidyapeetham University, Coimbatore campus-641 112, India*
[3]*Department of Production, Tata global beverage limited, Munnar-685 612, India*
[4]*Department of Computer Science and Engineering, Sri Ramakrishna Engineering College, Coimbatore, 641 022, India*

HIGHLIGHTS

Development of flat wire electrode as filler metal for GMAW to improve quality of weld bead

SCOPE OF WORK

- Development of experimental setup for continuous formation of flat wire electrode inline during GMAW process.
- Numerical analysis for electrical influences on flat wire electrode.
- Determination of flat wire electrode dimensions
- Experimental investigations on bead characteristics (weld bead geometry) of GMAW with flat wire electrode
- Study the effect of weld input process parameters on bead characteristics
- Analyze the transient thermal analysis of weld bead
- Investigated the mechanical and metallurgical characterization of weld bead

GRAPHICAL ABSTRACT

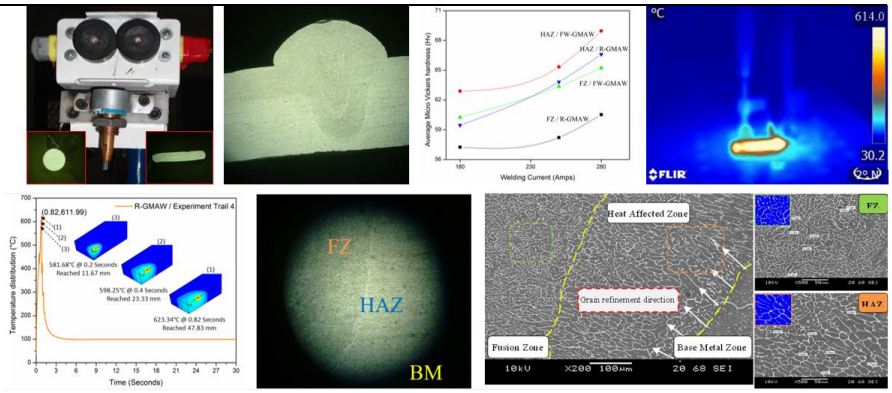

Abstract: This paper focusses on effect of flat wire electrode on gas metal arc welding (FW-GMAW) inline during the process to improve quality of weld bead. Since the flat wire electrode perimeter has enlarged, the turbulence of the molten droplet characteristics is altered due to the effect of electromagnetic force. To bring out, butt joint welding are proven with use of the flat wire electrode. The experimental results indicated that, the flat wire electrode and their orientations are significantly factors to improve the weld bead dimensions, due to the increased in steady state temperature and heat density. The end result also evident that the depth-to-width (D/W) ratio was improved on an average by 7.7 % than regular wire electrode used in GMAW. To validate, a comprehensive numerical model was developed, the result confirmed that the initial arc and steady state temperature are high for FW-GMAW. In addition, improvements in metallurgical and mechanical properties are discussed in this paper.

Keywords: Arc welding, flat wire electrode, electromagnetic force, depth-to-width ratio, and temperature distribution

1 INTRODUCTION

Globally, arc welding is one of the extremely booming and reliable methods of joining metals, which provides joints that are strong and reliable (1-2). One of the challenging areas as in GMAW is the study of transformation of molten metal (i.e. formation, detachment and impingement) between contact tip- to-work piece (3-5). Recent survey on arc welding indicated that the electrode tip geometry has a significant factor in enhancing the weldment quality by controlling welding current and electrode geometry size Chan et al. (6). Talabi et al. (7) & Tsai et al. (8) studied heat transfer and fluid flow analysis of the arc produced by flat and sharp electrodes was performed. They found that the arc velocity and pressure were low with the flat tip compared to the sharp tip and also Ushio and Masao et al. (Fukuhisa 1982) built a mathematical model to examine the various electrode shapes in arc welding, and concluded that the measured velocity reached the maximum with a sharp electrode tip. In the year of 2008 LI K H et al. (10) investigated double-electrode in gas metal arc welding (DE-GMAW) is to increase productivity. DE-GMAW is mainly because of overcomes the issues of tandem and variable pulse in GMAW. They found that, the consumable DE-GMAW can significantly increase the deposition rate by melting two welding wires, as a result of increasing the electromagnetic force. In the same year Shi Y et al (Shi et al. 2008) has modified the GMAW process into Dual-bypass gas metal arc welding (DB-GMAW). They observed that the bypass arcs have more significant in deciding the droplet transfer mode. Droplet neck shrinkage is enhanced by electromagnetic forces generated by bypass arcs, resulting in an increased anode area at the bottom of the droplet. As a result of neck shrinking and anode expansion, the detaching forces are increased. Fang Chen-fu et al. (12) performed TANDEM twin wire welding and twin wire GMAW. They concluded that the grain size in the heat-affected zone (HAZ) and joint strength were improved by the TANDEM weld. This is due to the droplet transfer, distribution on heat flow and interaction between two arcs being completely different from GMAW twin wire process. Especially, TANDEM had a narrower HAZ and finer microstructure than GMAW. Additionally, tensile strength increased by 5%. The studies in the literature show that electrode diameter and electrode tip geometry play a significant role in improving the efficiency of welding.

In contrast to the above approaches, the use of a flat electrode with optimized process parameters enables a good quality welding shape profile in GMAW which has been verified in current studies by Karuthapandi et al (13) and

`

Sripriyan et al. (14). Extension of that, weldment characterization of regular (cylindrical) and flat wire electrode on GMAW (R-GMAW & FW-GMAW) process is studied and confirm in this paper.

Butt joint welds are examined and their microstructural characteristics are predicted by creating a fuzzy logic model with respect to the input process parameter. The HAZ region will typically help to predict welding shape profiles accurately. Therefore, the weld bead shape together with the HAZ shape is considered the shape profile of the weld bead. In addition to that an Infra-Red camera is employed during the FW-GMAW, to measure the top surface transient temperature distribution.

However, experimental findings are frequently confined to welding technology, and the effect on wire electrode shape, and optimization strategies are ineffective when test parameters differ. As a result, defining thermal properties through pure experimental and optimization research is difficult. As a result, finite element analysis (FEA) can be used to precisely forecast welding temperature, cooling rate, microstructure, and residual stresses, among other things. Nezamdost et al. (15). In general welding processes involve the use of a concentrated heat source, which causes variations in time and space in the thermal field.

The equation for the transient temperature distribution for diverse heat sources in motion was initially developed by Rosenthal (16) and Rykalin (17). They proposed a heat source in the shape of a segments parallel to the weld axis and a segment perpendicular to it. In the year 1983 T W Eagar et al. (18) created a second-generation 2D Gaussian dispersed heat source and found a solution to the problem of a travelling heat source. To determine the transient temperature field, Bo K S et al. (19) used an analytical travelling Gaussian distribution solution. Ngyen et al. (20) found analytical solutions for the single and double ellipsoidal heat source models in temperature field simulation. To calculate the temperature field, Goldak et al. (21) built a finite elements model of a double ellipsoidal 3-D moving heat source. Aniruddha Ghosh et al (22) presented a new heat source model with a distinct form. They conclusion that a heat source with an oval form is acceptable for submerged arc welding. Various moving heat source models, such as the 2D disc technique, slit heat source, continuous heat input, arc heat flux, Gaussian heat distribution, and double ellipsoidal heat source, were discovered in the literature to investigate the improvement of weld bead in arc welding.

This paper also attempted to understand the thermal influence on weld bead characteristics. A 3D double ellipsoidal heat source shape model is created to estimate. The controlling heat transmission and elastic-plastic reaction equations are solved using a sequentially connected transient thermal static structural system. Material qualities that are temperature dependent, thermal and mechanical boundary conditions, the latent heat effect, and a double ellipsoidal volumetric heat source are all taken into account. The end analytical results are compared with different FW-GMAW experimental values.

The novelty of the work is the development of flat wire electrode as filler metals for gas metal arc welding to improve the quality of weld beads. For that, a new experimental setup was developed for the continuous formation of flat wire electrode inlines during GMAW process.

2 EXPERIMENTAL APPARATUS

2.1 Experimental set-up

Figure 1 displays the schematic configuration of the FW-GMAW system used in this study. There are three components that have been developed to perform the FW-GMAW process in the traditional GMAW process setup Karuthapandi et al. (1). The components are: modified wire feeder (MWF) mechanism, support wire feeder (SWF) mechanism, and new straight head welding torch. Power supply and gas supply systems are not included in the diagram. A modified wire feeder is used to give a flat shape to the electrode (Karuthapandi and Murugan 2017). The formation of flat wire electrode has been made possible with different types of loads applied by adjusting the wing nut shown in Figure 1. The driver roller of the modified wire feeder has a rectangular groove on the face, to form a flat wire electrode continuously with the required cross section (23). Figure 2 shows that the parts involved in the modified welding torch and support wire feeder is attached to horizontal arm which can be raised and lowered without loss of axial alignment when using tooling of different length (13). So it is possible to change a maximum distance of 250 mm between nozzles to the working portion. Similarly, horizontal motion can be controlled by a motor and the maximum length can operate approximately 300 mm. Therefore, only 300 mm of a weld bead length can possible to be achieved (1). The torch is equipped with gas inlet tube; the gas flow path is noted by the red dashed line in Figure 1. Since a straight head is used, it provides easy accessibility and weld visibility.

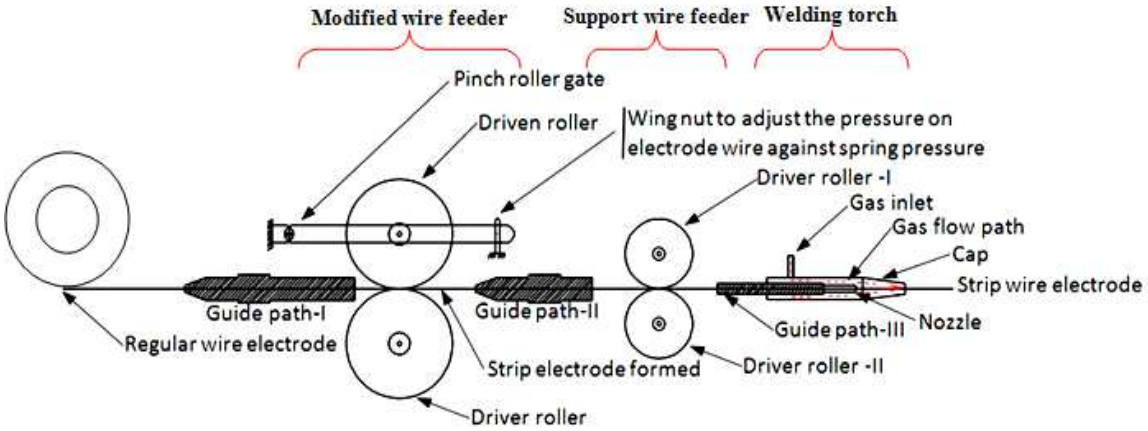

Figure 1 Schematic visualization of FW-GMAW setup

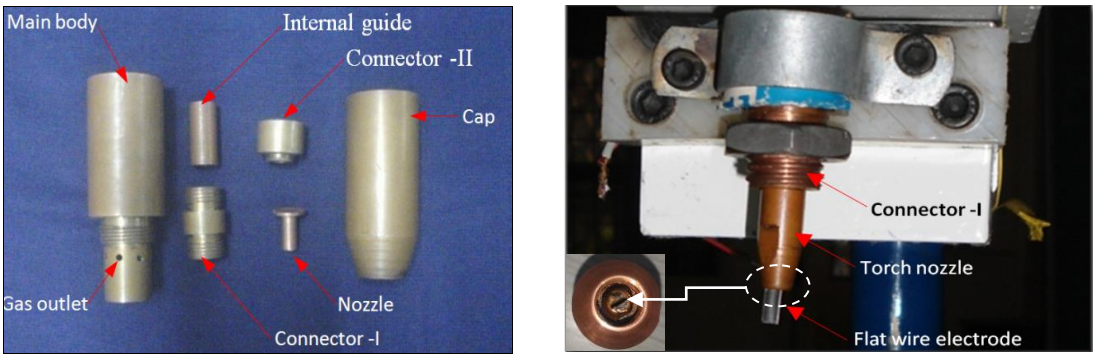

(i) Various parts in F W-GMAW torch **(ii)** View of flat electrode with FW-GMAW torch nozzle

Figure 2 Newly developed setup of FW-GMAW

2.2 Implication of flat wire electrode

Investigation was performed with AWS/ASTM A5.10: Al Si/5 Er4043 of 1.2 mm diameter as the control sample. Table 1 gives the chemical composition of the wire electrode. A variety of flat wire electrode size were achieved by the MWF system. Additionally the SWF and a modified wire killing roller system have been used in FW-GMAW, to continuously maintain the straightness of the flat wire electrode continuously (Kazeem K. Adewole 2012).

Table 1 Chemical composition of the wire electrode and base metal used, wt%

Materials used	Elements										
	Si	Fe	Cu	Mn	Mg	Cr	Zn	Ti	Al	Be	Other
Er 4043	4.5 -6	0.8	0.3	0.05	0.05	--	0.1	0.2	BAL	.0003	0.05–0.15
IS 6062	1.2	0.33	0.08	0.50	0.78	0.14	0.05	--	BAL	--	0.15

The investigation includes testing various geometries; the cross-sections of various flat wire electrodes to be tested were 1.4 x 1.1 mm, 1.5x 1.0 mm, 1.7 x 0.8 mm and 2 x 0.6 mm. However, the electrode geometry 2 x 0.6 mm is very close to the cross-sectional area of the cylindrical electrode as presented in Table 2. Therefore, the investigations focused only on a flat wire electrode with a geometry size of 2 x 0.6 mm. Figure 3 (i) shows the cylindrical and flat wire electrode and Figure 3 (ii-v) shows a macro view of the wire electrode geometry. The formed flat wire electrode suggests that, the perimeter of the flat wire electrode (2 x 0.6 mm) is 5.2 mm where the perimeter of the cylinder wire electrode is 3.77 mm, as shown in table 2.

Table 2 Different geometrical sizes of flat wire electrode

Wire electrodes	Dimension of wire electrode (mm)	Cross sectional area (mm^2)	Perimeter length (mm)
Regular electrode	Ø 1.2	1.13	3.77
Flat electrode	1.4 x 1.1	1.54	5.00
	1.5 x 1.0	1.50	5.00
	1.7 x 0.8	1.36	5.00
	2.0 x 0.6	1.20	5.20

However, the flat wire electrode perimeter was approximately 27.5% higher. The free space carries a high frequency current, while the welding current flows in the cylindrical wire electrode. If the frequency increases; the electrons move through the region of the surface rather than through the entire cross section, according to Sripriyan k et al. (13). With increased perimeter, it is possible to transfer more current with less resistance, which can help to increase welding speeds by changing the shape of the wire electrode Lancaster et al. (25). Therefore, the welding arc reached the entire width and fused completely along this width.

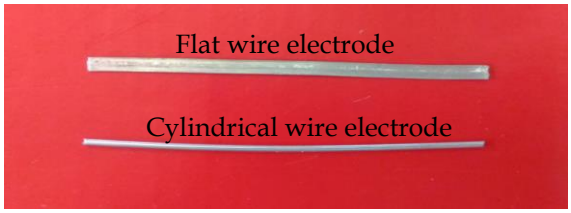

(i) View of deform wire electrode before and after

(ii) Macro view of cylindrical wire electrode

(iii) Macro view of formed flat electrode

(iv) Macro view of regular electrode with Ø1.2mm

(v) Macro view of formed flat wire electrode size of 2 x 0.6 mm

Figure 3 Details of electrode geometry shape before and after deform

The formation of weld metal droplets is governed by a variety of factors including the balance of forces acting on the droplet, the thermal electrode phenomenon, arc heat transfers and the current distribution of density in the droplet Tsai et al. (8). Hynes et al. (26) successfully investigated the formation of droplets, the detachment and impingement in gas metal arc welding on a molten pool. They concluded that as the welding current increased, means the transfer rate of droplets gradually increased. Nevertheless, current increases, the current density in the droplet's neck increases because of the decrease in the current-carrying zone, which causes the electromagnetic force acting on the droplet to increase. The electromagnetic force plays an important role in droplet detachment. Therefore, High Frequency Structure Simulator (HFSS) software was used to analyze the electromagnetic force by means of electric and magnetic fields in flat wire electrode. The distributions of electric and magnetic fields are shown in Figure 4 and % improvements were also calculated, welding current was considered a control factor. It is inferred that, increase in perimeter length increases in electric and magnetic fields. Approximately 47.57%, 33.81%, 36.1% and 18.99%, 24.63%, 20.22% for the electric field and magnetic field in welding current order, respectively, are detailed in Table 3. From this analysis; the welding current has a significant factor for both electric and magnetic fields. Increasing the welding current gradually increases and decreases the electric and magnetic fields. Further electrode length also one the predominant effect on electric and magnetic fields. Thus the use of flat wire electrode in GMAW can improve the weld bead characteristics; which has not been verified by any of the investigators.

Table 3 Comparison of electric and magnetic fields for regular and flat wire electrode

Welding current (amp)	Stick out distance (mm)	Electric field (volts parameter)			Magnetic field (Gauss)		
		Regular electrode	Flat electrode	% of improvement	Regular electrode	Flat electrode	% of improvement
180		3.105	5.922	47.57	1.309	1.616	18.99
240	15	3.011	4.549	33.81	1.328	1.762	24.63
280		3.078	4.817	36.10	1.341	1.681	20.22

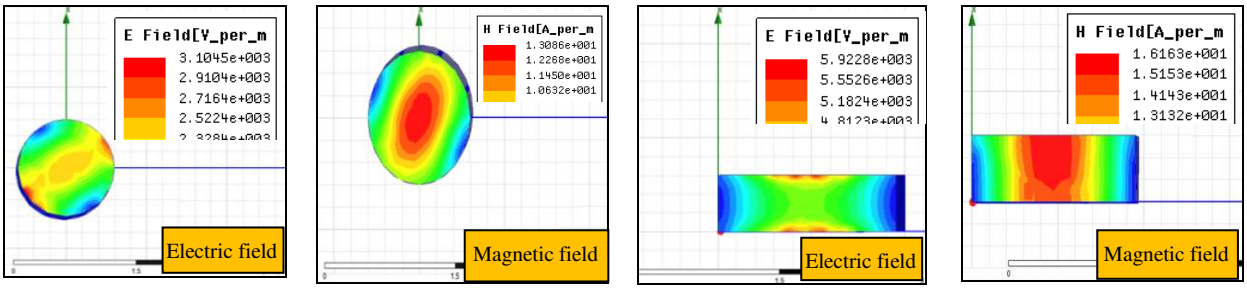

(i) Electric and magnetic field of regular and flat wire electrode at 180 A

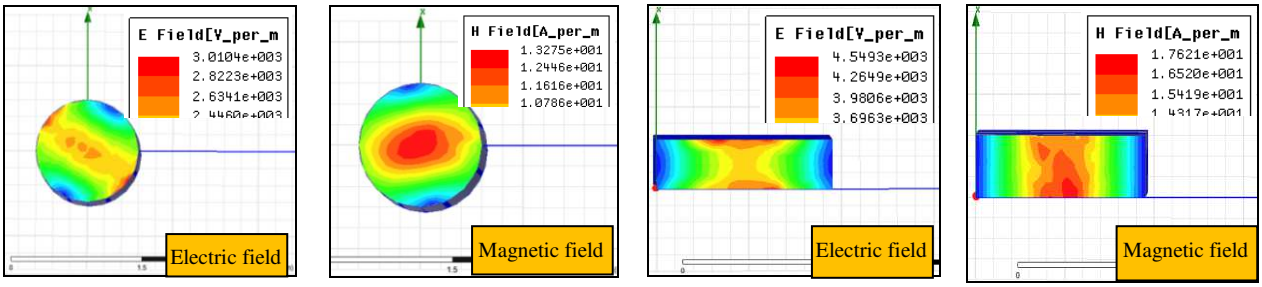

(ii) Electric and magnetic field of regular and flat wire electrode at 240 A

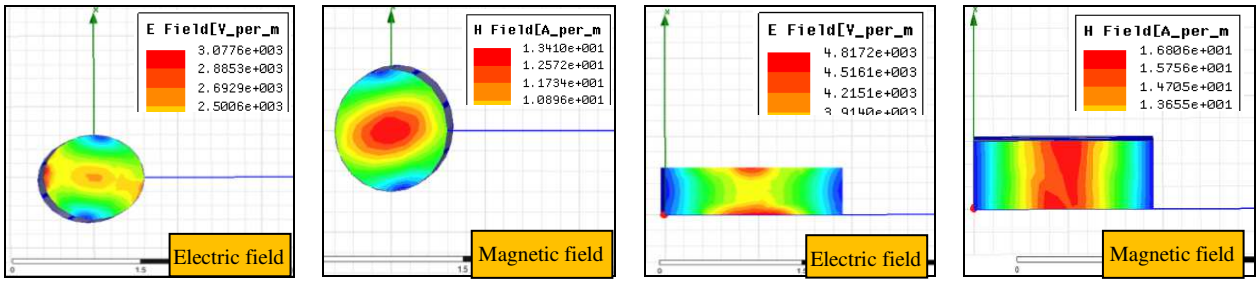

(iii) Electric and magnetic field of regular and flat wire electrode at 280 A

Figure 4 Distribution of the electric and magnetic field of the regular and flat wire electrode

2.3 Process parameters and flat wire electrode orientations

Aluminum AA6061 alloy plates with dimensions 100 mm x 25 mm x 10 mm are used as base metals for this study. Aluminum 6061 is used in marine, automotive and aerospace applications where strength and corrosion resistance are very high priorities. The key independent parameters defined for this investigation are welding current *(I),* welding speed *(WS),* orientation of flat electrode *(θ)* and wire feed rate *(F).* the wire feed rate (*F*) was found to be directly proportional to the welding current (*I*). Therefore, it is considered to be an independent parameter Das J E R et al. (27). The selected welding input process parameters and their levels are presented in Table 4.

Table 4 Welding parameters and their levels

Parameters	Level 1	Level 2	Level 3
Welding current I *(A)*	180	230	280
Welding Speed WS *(mm min^{-1})*	350	430	500
Flat wire electrode orientations *(θ)*	0°	45°	90°

Different welding results can be obtained in FW-GMAW, depending on whether a flat wire electrode has fed parallel to the direction of welding (0°), inclined to the direction of solder (45°), and normal to the direction of solder (90°) and the influence of these three orientations on the structure of the flat wire electrode. The Figure 5 shows the orientation of the flat electrode used in this study with respect to the welding direction.

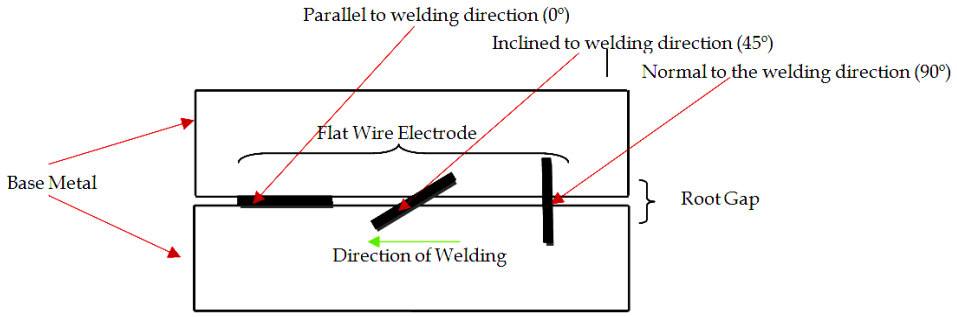

Figure 5 Orientations of flat wire electrode

3 EXPERIMENTAL OBSERVATIONS AND PREDICTIONS

3.1 Analyses of weldment characteristics

The experimental trial runs were conducted; argon gas was used as a shielding gas and supplied at a constant flow rate of 20 liters per minute and a stick out distance of 15 mm. After welding, the best quality of the weld specimens was obtained by sectioning and polishing. The weldment profiles were traced using an optical projector, and Figure 6 shows the typical welded samples. The weld bead dimensions are measured such as bead width and total width of the weldment, reinforcement height, penetration depth and depth of the HAZ. These data are utilized to obtain a smooth curve fitting of the weldment shape profile geometry.

(i) inclined to the welding direction (expt. trial -2)

(ii) Normal to the welding direction (expt. trial -3)

(iii) inclined to the welding direction (expt. trial -4)

(iv) Parallel to the welding direction (expt. trial -1*)

(v) Normal to the welding direction (expt. trial -7)

(vi) inclined to the welding direction (expt. trial -8)

(a) FW- GMAW

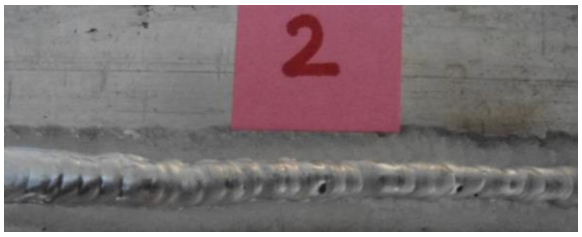

(i) Regular welding (expt. trial -2)

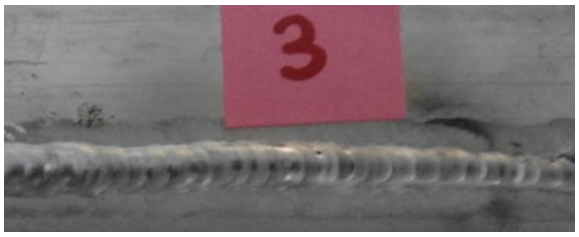

(ii) Regular welding (expt. trial -3)

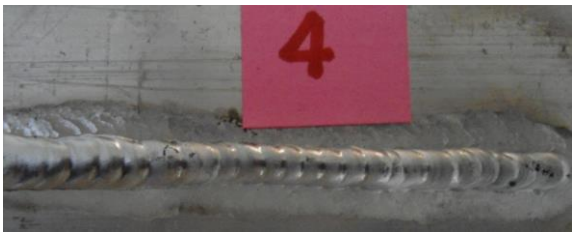

(iii) Regular welding (expt. trial -4)

(iv) Regular welding (expt. trial -6)

(v) Regular welding (expt. trial -7)

(vi) Regular welding (expt. trial-8)

(b) R-GMAW

Figure 6 Macroprofile of the top surface morphologies

Table 5 FW-GMAW responses of weld bead characteristics on different experimental trials

Trial.	Welding parameter's			Measured values of weld bead characteristics (mm)											
	Welding Current (I)	*Welding Speed (WS) mm/min*	*Electrode Orientation (θ)*	*Weld bead width (BW)*	*Total weld bead width (BW + HAZ W))*	*Height of reinforcement*			*Depth of Penetration*			*Depth of HAZ*			*D/W ratio*
						R_1	R_2	R_3	P_1	P_2	P_3	H_1	H_2	H_3	
1	180	350	0°	8.2	9.8	3.20	2.80	1.60	4.90	4.00	2.10	1.38	1.50	1.68	0.60
2	180	430	45°	7.8	8.8	2.40	2.00	1.20	4.10	3.50	2.00	1.10	0.95	1.50	0.53
3	180	500	90°	7.4	8.0	2.60	2.12	1.32	3.40	2.80	1.25	1.10	0.95	1.25	0.46
4	230	350	45°	8.6	9.5	2.28	2.08	1.10	3.45	3.10	1.50	1.50	0.92	1.20	0.40
5	230	430	90°	8.0	9.2	2.52	2.00	1.20	3.50	3.15	1.25	1.12	0.96	0.95	0.44
6	230	500	0°	8.8	9.4	3.20	2.40	1.15	3.80	3.00	2.15	1.10	1.00	2.00	0.43
7	280	350	90°	7.8	8.6	2.40	2.40	1.10	3.30	2.80	1.40	1.50	1.20	1.00	0.42
8	280	430	0°	8.6	9.3	2.80	2.80	1.30	3.70	3.00	2.16	1.25	1.00	1.50	0.43
9	280	500	45°	8.4	9.0	2.20	2.00	1.10	3.45	2.85	1.60	1.00	0.94	1.00	0.41

Table 6 R-GMAW responses of weld bead characteristics on different experimental trials

Trial.	Welding parameter's			Measured values of weld bead characteristics (mm)											
	Welding Current (I)	*Welding Speed (WS) mm/min*	*Electrode Orientation (θ)*	*Weld bead width (BW)*	*Total weld bead width (BW + HAZ W)*	*Height of reinforcement*			*Depth of Penetration*			*Depth of HAZ*			*D/W ratio*
						R_1	R_2	R_3	P_1	P_2	P_3	H_1	H_2	H_3	
1	180	350	Neglected parameter	7.5	8.2	2.40	1.60	1.10	3.30	2.91	1.10	0.80	1.12	1.00	0.44
2	180	430		7.0	7.6	1.60	1.10	0.91	3.00	2.65	1.10	0.60	0.50	0.93	0.43
3	180	500		6.5	7.2	1.80	1.30	0.90	2.42	1.62	0.52	0.61	0.45	0.50	0.37
4	230	350		7.7	8.0	2.28	1.40	0.84	2.56	2.10	0.89	1.00	0.48	0.45	0.33
5	230	430		7.2	7.7	1.50	1.21	0.80	2.80	2.31	0.70	0.55	0.50	0.38	0.39
6	230	500		7.8	8.1	1.70	1.30	0.61	3.10	1.46	1.30	0.52	0.80	1.21	0.40
7	280	350		6.6	7.6	1.50	1.42	0.60	2.50	1.70	0.60	0.98	0.81	0.61	0.38
8	280	430		8.3	7.1	1.20	1.70	0.79	2.82	2.00	1.21	0.74	0.75	0.51	0.34
9	280	500		7.6	7.9	1.00	0.98	0.81	2.76	1.94	0.90	0.49	0.52	0.58	0.36

3.2 Study on weld bead geometry

The macrostructure responses are measured and tabulated in Tables 5 and 6. The weld bead width, total weld bead width (including the width of the HAZ), reinforcement height, penetration depth and HAZ depth ranged from 7.4 to 8.8 mm, 8 to 9.8 mm, 1.77 to 2.53 mm, 2.48 to 3.67 mm and 0.98 to 1.52 mm respectively for FW-GMAW. Similarly, 6.5 to 8.3 mm, 7.1 to 8.2 mm, 0.93 to 1.7 mm, 1.52 to 2.44 mm and 0.48 to 0.97 mm in for R-GMAW. Due to the increases in weldment shape, the depth to width ratio was calculated for all the weld samples. The welded samples do not show welding cracks or porosity; this may be due to perfect orientation and size of the flat electrode, good crack resistance of the base metal and proper welding conditions. Regarding the increased volume of weldment shape, the analysis results show that the flat wire electrode is the most prominent factor, while the other two have least significant.

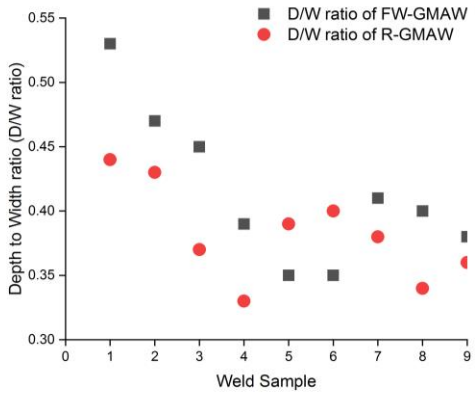

Figure 7 Comparison of depth-to-width ratios

The Figure 7 insist that the depth-to-width (D/W) ratio in both FW-GMAW and R-GMAW had comparable patterns. In experimental order, the differences in the D/W ratios are 27%, 19 %, 20%, 18%, 11%, 7%, 10%,21%, and 12%. As the welding current, the depth-to-width ratio falls as welding speed increases. This is because, with constant welding current, the energy input to the base metal reduces as the welding velocity rises. Welding conduction is the primary process involved when the energy input is minimal, resulting in a significant conduction loss and a low depth to width ratio. The input energy can be increased by increasing the perimeter of the flat wire electrode to obtain a linear energy input that helps to increase the depth-to-width ratio.

3.3 Experimental temperature distribution of FW/R-GMAW

The objective of the analysis is to understand the transient temperature behavior during FW-GMAW and its influence on weld bead dimensional profile. Since perimeter of the flat wire electrode is greater, a higher rate of input heat is generated. Due to increased heat input, there is an increase in electrode wire melting rate. Therefore, the current density in the droplet's neck increases because of the decrease in the current-carrying zone Gery et al. (28). This current density causes the electromagnetic force acting on the droplet to increase the velocity of the droplet; resulting in increased number of droplets and maximum temperature exists in the FZ with less time, which may increase the volume of the FZ. Two different temperature acquisition methods are used in FW-GMAW and R-GMAW processes. In the first method, the peak temperature was acquired under

`

the weld bead on the weld line using thermocouples. In parallel, the temperature distribution was acquired on weld pool top surface using thermal image camera.

For this investigation, K-type (chromel-alumel) thermocouples are instrumented prior to the process. This is inexpensive and is available with a wide variety of probes. The range of thermocouples used for experimentation is from 1°C to 1200°C. Two thermocouples (T_1 & T_2) are used which is fitted into a 6 mm blind hole of 1.5 mm diameter that are produced 15 mm from either side of the welding line. The measurement points are located in the bottom of the centerline of weld plate which is considered to be the under-bead temperature. For every 0.25 second, data of the selected points are recorded, the average peak under bead temperature details are in Table 7.

Table 7 Temperature difference on R-GMAW and FW-GMAW process

Exp. trials	R-GMAW		FW-GMAW		% of temp. difference between R-GMAW Vs FW-GMAW	
	Under bead Temperature (˚C)	Peak surface Temperature (˚C)	Under bead Temperature (˚C)	Top surface Temperature (˚C)	% of under bead emperature difference	% of peak surface temperature difference
1	598.00	608	645.65	649	7.38	6.32
2	581.58	591	617.10	629	5.76	6.04
3	578.54	588	601.30	612	3.79	3.92
4	604.69	618	635.00	650	4.77	4.92
5	594.58	602	622.00	632	4.41	4.75
6	581.83	589	615.80	626	5.52	5.91
7	613.58	619	634.00	642	3.22	3.58
8	593.64	601	624.00	629	4.87	4.45
9	586.75	592	609.00	619	3.65	4.36

The thermocouple results inferred that the range of peak temperatures was 601.3 - 645.65˚C and 578.54 - 613.58˚C in FWGAMW and R-GMAW respectively. The temperature is slightly greater with use of FW-GMAW process. The overall percentages of improvements are 7.38, 3.28, 7.74, 5.81, 3.45, 7.20, 3.22, 3.65, and 5.92 % in design of experiment order. It is evident that the maximum temperature recorded is little higher in the case of 0° orientation of the flat wire electrode and followed by 45° and 90° respectively. Temperature distribution is nearly constant with the electrode orientations of 45° and 90°.

However, to obtain more accurate results, infrared thermography is used as an alternative method for this study, detailed in Figure 8. For this study the emissivity (ε) value is calculated and confirmed by literature survey as 0.42 by equation 1 Frappier et al. (29) & M.C. Zondi et al. (30).

The surface peak temperature on the weld line is recorded and tabulated in Table 7. The percentage of surface temperature improvement is calculated as 6.32, 6.04, 3.92, 4.92, 4.75, 5.91, 3.58, 4.45 and 4.36 % in the experimental order. Furthermore, trial cases of 4, 5 and 6 for FW-GMAW and trial case 4 for R-GMAW are considered for comparison. With the same input parameter condition, the trial case 4 have 650˚C and 618˚C as maximum weld surface temperature for FW-GMAW and R-GMAW processes. Due to increase in temperature, the weld bead profile improves approximately 8.64 %. Similarly, the trial cases 5 and 6 have improved weld bead area of approximately 22.97 % and 25.76 % respectively.

$$\frac{\varepsilon//+\varepsilon\perp}{2}=\varepsilon \quad (1)$$

Where ε// and ε⊥ are calculated by

$$\varepsilon_{//}=\frac{4n\times\cos(\theta)}{(n^2+k^2)\times\cos^2(\theta)+2n\times\cos(\theta)+1}$$

$$\varepsilon_{\perp}=\frac{4n\times\cos(\theta)}{\cos^2(\theta)+2n\times\cos(\theta)+n^2+k^2}$$

`

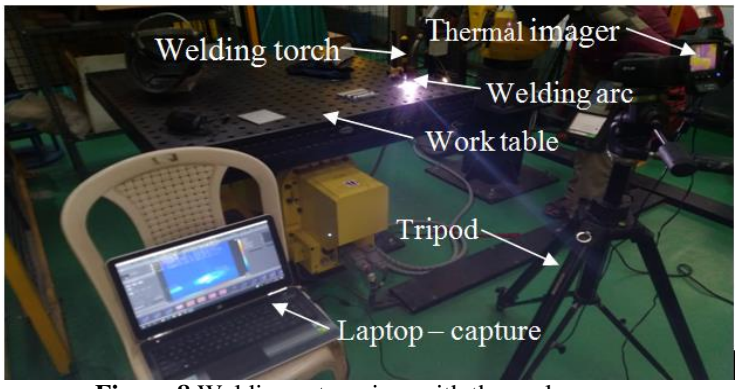

Figure 8 Welding setup view with thermal camera

In addition the result inferred that influence of the flat wire electrode orientation is one of the significant parameters. Thus, the weld parameters such as weld bead width and penetration depth is slightly higher for 0˚ orientation thans other two orientations. For example, considering the trial cases 4, 5 and 6, approximately 7% of weld bead area has been improved. In real practice, 0˚ orientation of flat wire electrode is more preferable for applications using high penetration depth whereas 45˚ and 90˚ orientations are preferable for high bead width applications.

Transient analysis is performed after the process, to understand the temperature difference in different periods of time as detailed in Figures 9-12. At 25s the temperature is 598˚C, 583˚C, 540˚C and 538˚C for FW-GMAW (45˚, 90˚ and 0˚) and R-GMAW processes respectively. Similarly, at 0.45s the temperature in above cases observed as 629˚C, 587˚C, 568˚C and 573˚C respectively. The maximum temperature is attained at 75s for 45˚ orientation, 175s for 90˚ orientation, and 225s taken for 0˚ orientation and regular wire electrodes.

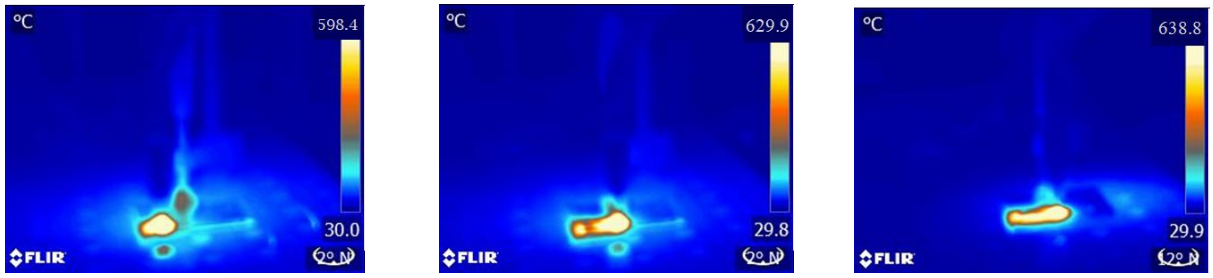

(i) at12 milliseconds (ii) at 45 milliseconds (iii) at 75 milliseconds

Figure 9 Thermography image set in FW-GMAW with 45˚electrode orientation (trial case 4)

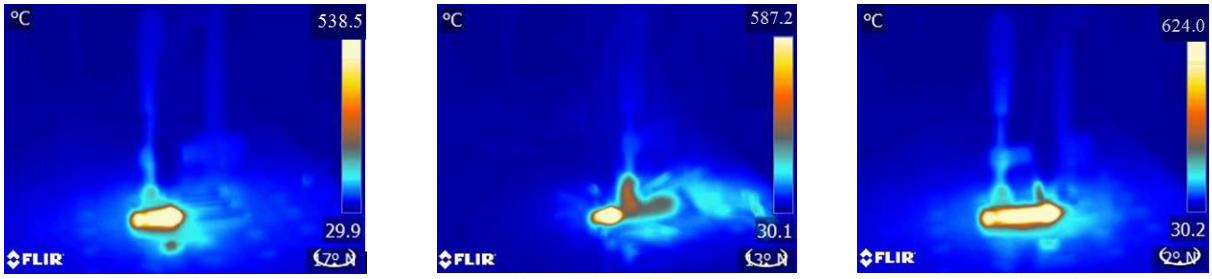

(i) at 12 milliseconds (ii) at 45 milliseconds (iii) at 105 milliseconds

Figure 10 Thermography image set in FW-GMAW with 90˚ electrode orientation (trial case 5)

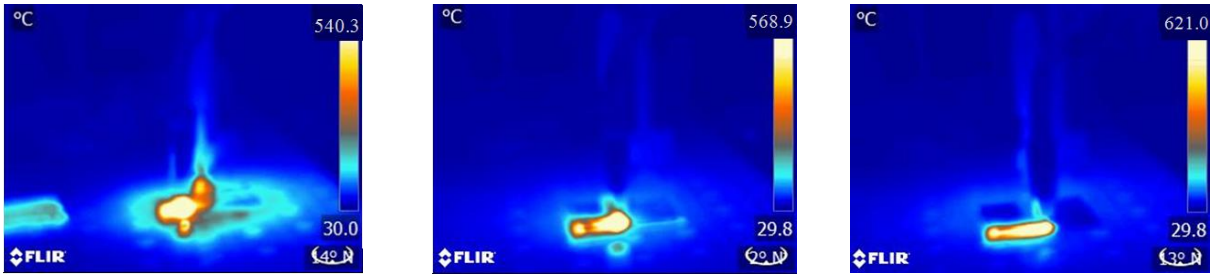

(i) at12 milliseconds (ii) at 45 milliseconds (iii) at 135 milliseconds

Figure 11 Thermography image set in FW-GMAW with 0˚ electrode orientation (trial case 6)

`

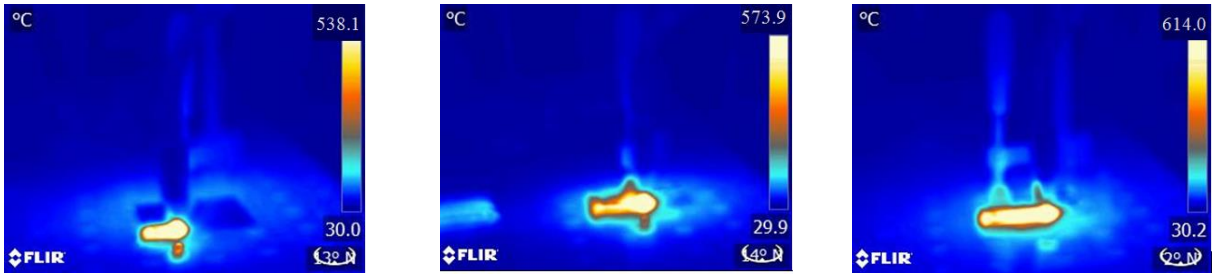

(i) at 12 milliseconds (ii) at 45 milliseconds (iii) at 135 milliseconds

Figure 12 Thermography image set in R-GMAW (trial case 4)

3.4 Modeling and analysis of weldment

Fuzzy logic is one of the successful soft computing techniques of fuzzy set theory Rane (31). A fuzzy model was developed in this paper to predict the significance of input parameter and their related output. The membership functions are numerical functions corresponding to linguistic terms (32). The triangular membership function is selected for this paper, which is most suited for real time application and very less computational requirements (Bandler W 1988). Usually the fuzzy logic input and output variables are quantized into sets of classes defined by linguistic labels. Both the inputs and output were quantized into three fuzzy sets for this experiment, namely: Low, Medium, and High.

The triangular membership function may be shown as follows

$$\mu(X) = \begin{cases} 0 & for \quad x \le \alpha \\ \dfrac{x-a}{b-a} & for \quad a \le x \le b \\ \dfrac{c-x}{c-b} & for \quad b \le x \le c \\ 0 & for \quad c \le 0 \end{cases} \qquad \text{---------- (2)}$$

where $\mu(X)$ is referred to as the membership function and the indexes a, b and c indicate the crisp values of triangular me mbership functions.

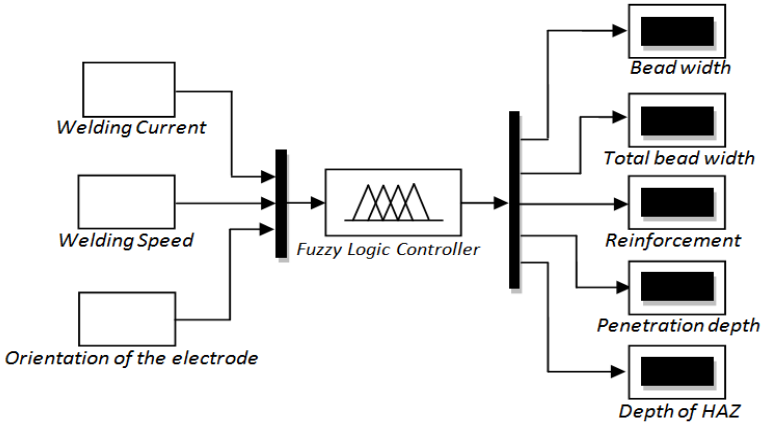

Figure 13 Structure of fuzzy logic simulation model

The simulation was performed using three input parameters and the simulation purpose was to predict the five outputs for the experiments. Figure 13 shows the SIMULINK model, was developed to predict the output of FW-GMAW macrostructure characteristics. The measured and predicted values are compared manually. The maximum deviation was shows in the case of reinforcement and penetration zones since it is very difficult to measure accurate boundaries of R_1 and P_1 of weldments. The experimentally observed values and predicted values of SIMULINK were used for graphical representation of the weldment cross section shape profiles presented for all trial cases shown in Figure 14. The individual orientation of the flat wire electrode is studied and compared with R-GMAW, details in Table 8.

Therefore, the use of flat electrode is one of the better options for enhancing the macrostructure characteristics of weldments in the GMAW process.

Table 8 % of macrostructure characteristics improvement

Electrode Orientation (θ)	Avg. % of Bead width (BW)	Avg. % of Total width (BW + HAZ W)	Avg. % of Reinforcement height	Avg. % of Penetration depth	Avg. % of Depth of HAZ
0°	7.81	17.89	41.65	33.36	39.97
45°	10.08	13.92	33.25	29.94	45.10
90°	12.50	12.79	37.54	33.61	46.26
Over all	10.05	14.95	37.54	34.85	43.02

`

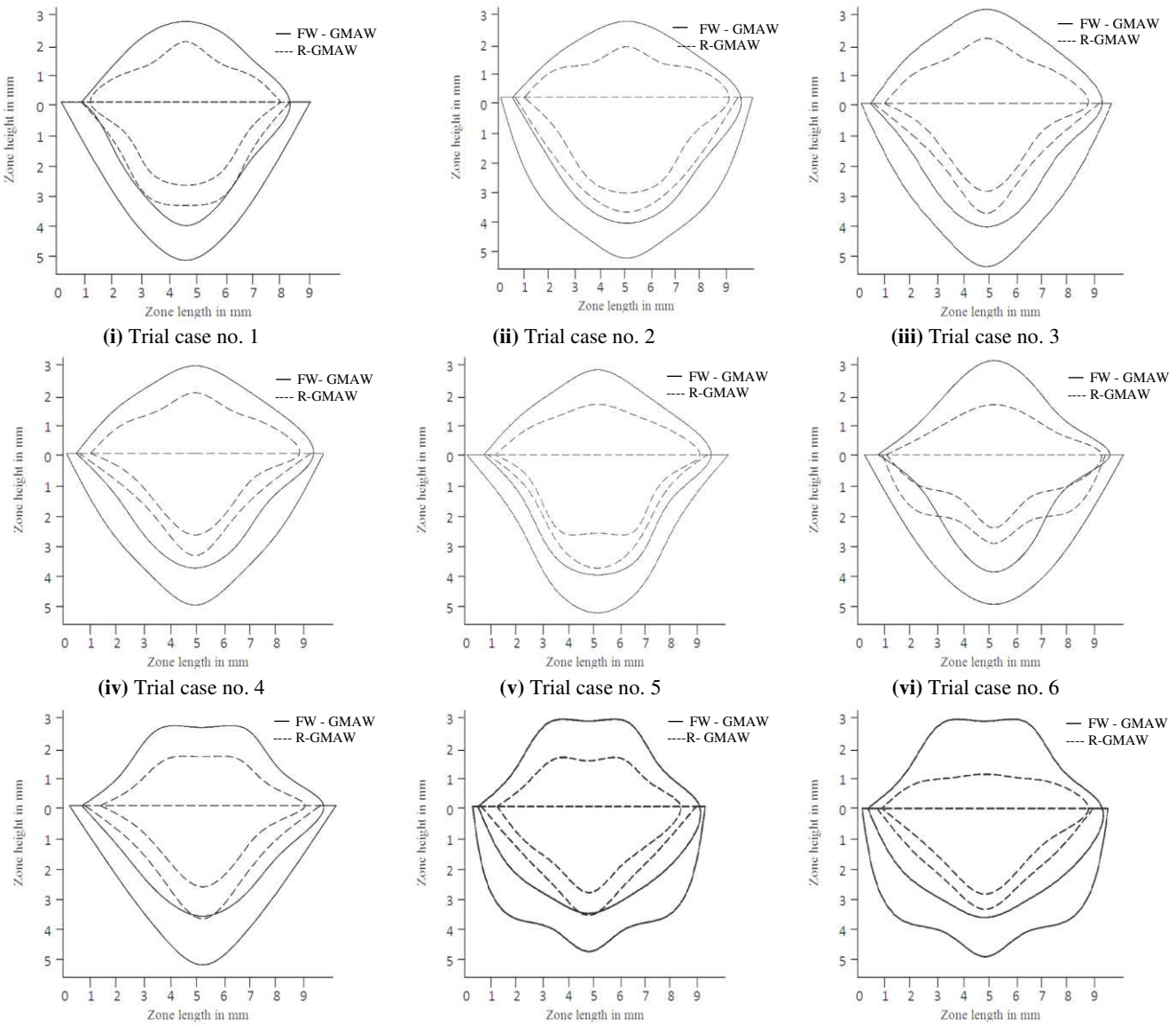

(i) Trial case no. 1 **(ii)** Trial case no. 2 **(iii)** Trial case no. 3

(iv) Trial case no. 4 **(v)** Trial case no. 5 **(vi)** Trial case no. 6

(vii) Trial case no. 7 **(viii)** Trial case no. 8 **(ix)** Trial case no. 9

Figure 14 Typical weldment shape profile trial case

4 NUMERICAL ANALYSIS

4.1 Heat transfer simulation

The objective of this chapter is to create a complete numerical model that can anticipate the temperature distribution that occurs during the gas metal arc welding process while using a flat wire electrode (FW-GMAW). Due to the action of electromagnetic force, the turbulence of the molten properties has changed since the electrode geometry has changed from the typical geometry. As a result, the droplet neck's current density rises as the current transmission area shrinks Gery et al. (28). This current density permits the droplet's velocity to be increased by the electromagnetic force acting on it, resulting in an increase in the number of droplets and maximum temperature in the FZ, which can increase the FZ's volume. As a result, a thorough numerical model is created to forecast the temperature distribution that occurs during the gas metal arc welding process using the flat wire (FW-GMAW) electrode.

Rosenthal [16] developed the first analytical model of moving heat sources to understand the thermal history of welds. In general, the linear heat conduction equation for the welding process consists of

$$\left\{\begin{array}{c}\text{Heat conduction}\\ \text{at x, y, and z}\end{array}\right\}-\left\{\begin{array}{c}\text{Heat conduction}\\ \text{at x + }\Delta\text{x, y +}\\ \Delta\text{y, and z + }\Delta\text{z}\end{array}\right\}+\left\{\begin{array}{c}\text{Heat generation}\\ \text{inside the}\\ \text{element}\end{array}\right\}=\left\{\begin{array}{c}\text{Heat}\\ \text{accumulated of}\\ \text{the element}\end{array}\right\}$$

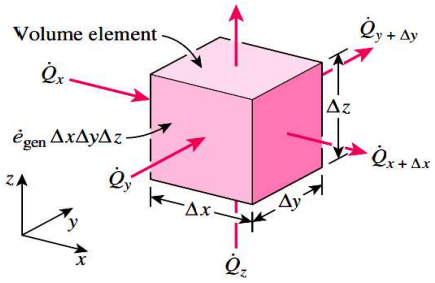

Figure 15 3D Heat conduction through a rectangular element

Consider a element of length Δ_x, width Δ_y, and height Δ_z, as shown in Figure 15 and energy balance on this element during time interval $\Delta t \rightarrow 0$ can be expressed in equation 3.

$$\dot{Q_x} + \dot{Q_y} + \dot{Q_z} - \dot{Q}_{x+\Delta x} - \dot{Q}_{y+\Delta y} - \dot{Q}_{z+\Delta z} + \dot{E}_{eng.element} = \frac{\Delta E_{element}}{\Delta t} \quad (3)$$

Volume of element is $=\Delta_x\Delta_y\Delta_z$ and the respective heat transfer areas of the x, y, and z direction are $A_x=\Delta_y\Delta_z$, $A_y=\Delta_x\Delta_z$ and $A_z=\Delta_x\Delta_y$.The fundamental heat transfer partial differential equation is as follows in equation 4 (34) & (35):

$$\frac{\partial}{\partial x}\left(k\frac{\partial T}{\partial x}\right) + \frac{\partial}{\partial y}\left(k\frac{\partial T}{\partial y}\right) + \frac{\partial}{\partial z}\left(k\frac{\partial T}{\partial z}\right) + \dot{E}_{eng.element} = \rho c_p \frac{\partial T}{\partial t} \quad (4)$$

where T (x, y, z, t) is the temperature, $\dot{E}_{eng.element}$ is rate of internal heat generation, t is the time, ρ is the density, c_p is the specific heat, k is the thermal conductivity in x, y and z directions respectively. In the mathematical model, initial temperature is considered as T_0=30˚C with condition of T (x, y, z, t) = T_0 (x, y, z). Equations 5 and 6 expressed the heat convection and radiation is considered for the study.

$$q_{(x,y,z,t)_{convection}} = h(T - T_0) \quad (5)$$

$$q_{(x,y,z,t)_{Radiation}} = \varepsilon\sigma(T^4 - T^4{}_0) \quad (6)$$

where σ is the Stefan-Boltzmann constant = $5.67\text{x}10^{-8}\text{Wm}^{-2}$ ˚C^{-4}; h and ε are the convection coefficient, and emissivity respectively. Convection is caused by the a flow of shielding gas (pure argon) with flow rate of 20 liters per meter. The temperature dependent properties of the selected Al material are tabulated in Table 9 which shows the thermal conductivities, specific heat capacities, and density are obtained from the literature.

Table 9 Temperature dependent properties of aluminum alloy 6061

Material	Melting rang (°C)	Temperature (°C)	Thermal conductivity (W/m°C)	Heat capacity (J/kg°C)	Density (kg/m^3)
Al6061	576-664	0	104	673	2789
		121	96	705	2749
		242	87	755	2699
		338	77	805	2660
		465	68	860	2613
		585	57	957	2575
		628	47	983	2529
		651	35	1025	2492

4.2 Moving heat source model

To understand the temperature behaviours of both R-GMAW and FW-GMAW, numerical simulation was performed using ANSYS Parametric Design Language (APDL) mode. During the transient analysis, the location of the heat source center changes at different time steps. According to a review of the literature, a birth-and-death element technique is commonly used to monitor weld-element activation as the heat source progresses. Metal develops in accordance with the position of the moving heat source as the welding progresses (Sripriyan et al. 2021) & (Bai-Qiao Chen 2016). To obtain an accurate temperature gradient, higher temperature gradients are expected in and around the fusion zone (FZ) and heat affected zone (HAZ). In the region of highest temperature gradient, the finite element mesh is graded finest, while outside the heating zone, a coarse mesh is used. Figure 16 depicts the model's detailed dimensions as well as a symmetric view of various meshes along the weld line. This analysis makes use of the 8 noded SOLID70 hexahedron element type. For all trial cases, the mesh size along the welding line (y-axis) is 0.5 mm, the mesh size along the plate width (x-axis) is 1 mm, and the mesh size along the plate thickness (z-axis) is 0.75 mm. The fine mesh is used in the FZ area to obtain greater accuracy when moving heat sources at specific times (t).

`

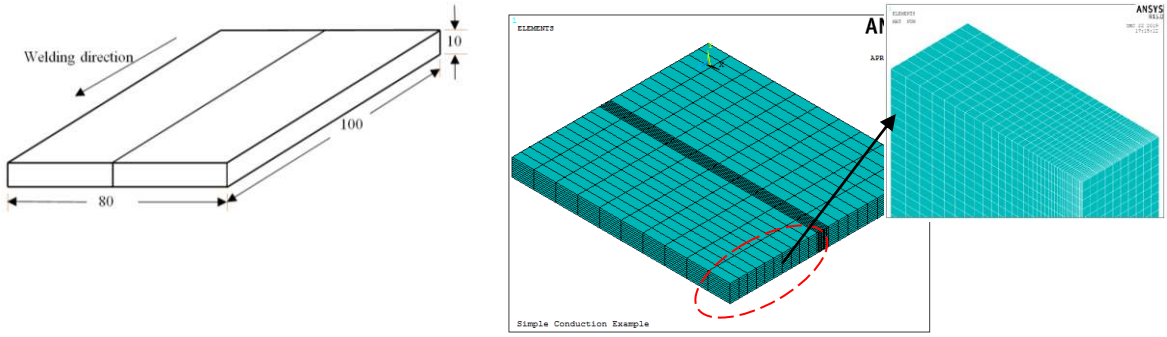

Figure 16 Dimension of weld joint and finite element model

The thermal behaviour of the fusion zone is predicted using a double ellipsoidal model of source heat in this study. Figure 17 (a-c) depicts the distribution of volumetric heat density over a double ellipsoidal space. Figure 17 (d-g) depicts the developed double ellipsoidal shaped finite element region and various views subjected to the heat generation rate defined by equations 7 and 8 at a specific time (t).

Goldak's double ellipsoidal heat source model is widely used to describe thermal behavior in many commercial welding processes. To understand the thermal behavior of FW-GMAW, Goldak's model employs a double ellipsoidal heat source equation, as shown below.

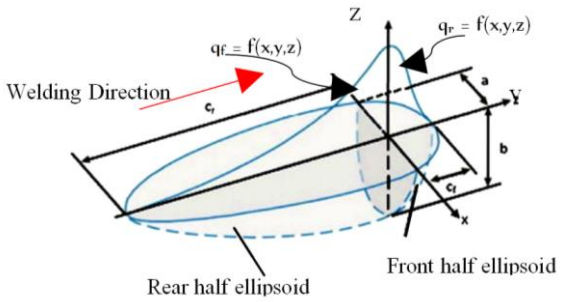

(a)3D heat conduction volume element and power density distribution inside the double ellipsoid

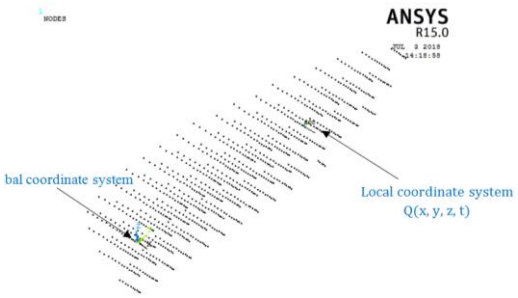

(d) Double ellipsoidal heat source region

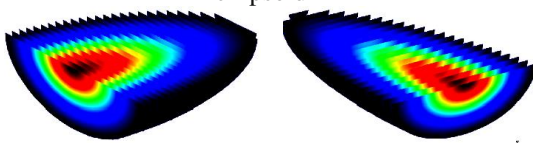

(b) Front ellipsoidal model

(c) Rear ellipsoidal model

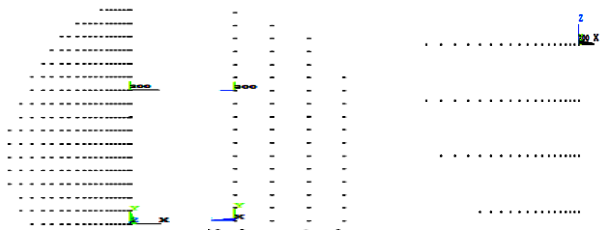

(e) Front side (f) Right side (g) Bottom side

Figure 17 Different views of Goldak heat source model and selected nodes in double ellipsoidal region

$$P_{(x,y,z,t)Front} = \frac{-6\sqrt{3}\,Qf_f}{\pi\sqrt{\pi}\,abc_f}\, e^{-3\left(\frac{(x-x_0)^2}{c_f^2} + \frac{(y-y_{00})^2}{a^2} + \frac{(z-z_0)^2}{b^2}\right)},\quad y\geq 0 \tag{7}$$

$$P_{(x,y,z,t)_{Rear}} = \frac{-6\sqrt{3}\,Qf_r}{\pi\sqrt{\pi}\,abc_r}\, e^{-3\left(\frac{(x-x_0)^2}{c_r{}^2} + \frac{(y-y_{00})^2}{a^2} + \frac{(z-z_0)^2}{b^2}\right)},\quad y<0 \tag{8}$$

$$f_f + f_r = 2 \quad and \quad \frac{f_f}{c_f} = \frac{f_r}{c_r} \tag{9}$$

$$Q(x,y,z,t) = \begin{cases} P_{(x,y,z,t)_{Front}} & \text{for } y \geq y_{00} \\ P_{(x,y,z,t)_{Rear}} & \text{for } y < y_{00} \end{cases} \tag{10}$$

P's are heat densities in W/m^3 at any spatial point (x, y, z) at any time t inside the front (f) and rear (r) half-ellipses. Weld bead geometric parameters a, b, and c are shown in Figures 18 and 19, with parameter c assuming the lengths of c_f and c_r for the front and rear half-ellipsoid. To ensure continuity, the total energy input rate Q (VI in watts) is divided into fractions f_f and f_r, and the fraction of heat deposition parameters satisfy equation 9. y_{00} is the transformation between the fixed and moving coordinate systems, and it is equal to y_0 +vt, where v is the welding speed (m/s). Equation 10 represents the net heat input accumulated on the weld surface at any time.

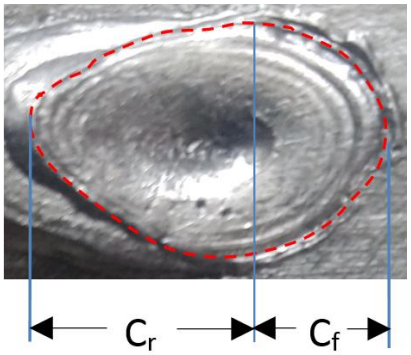

a) 0° orientation of FW-GMAW (trial case 6)

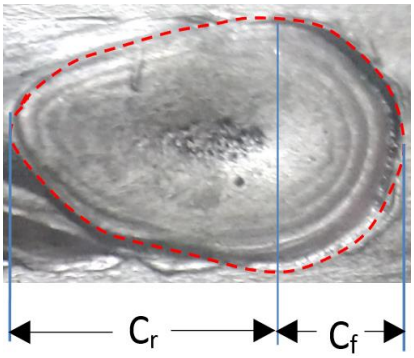

b) 45° orientation of FW-GMAW (trial case 4)

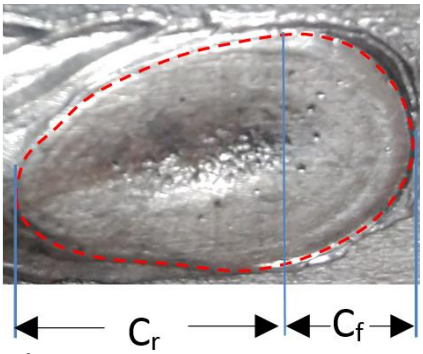

(c) 90° orientation of FW-GMAW (trial case 5)

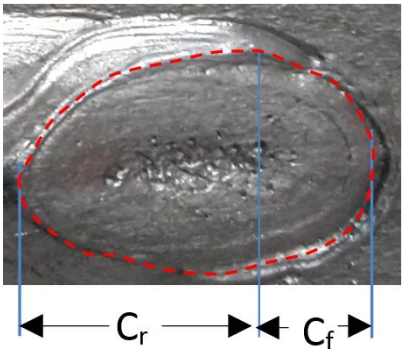

(d) Regular welding of R-GMAW (trial case 4)

Figure 18 Data Acquisition for weld crater measurement of power density in front and rear ellipsoidal

`

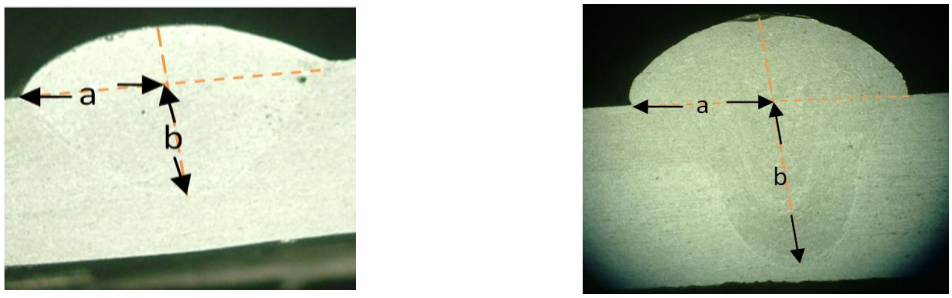

Figure 19 Data Acquisition Measures of half width and depth from welded samples

4.3 Transient temperature distribution response

The contours of the temperature distributions of both FW-GMAW and R-GMAW processes are obtained from the simulated results. The purpose of this analysis is to understand the transient temperature behavior during the FW-GMAW process and its effects on the weld bead dimensional profile Kong, F et al. (38) & Fanrong Kong et al (39). Figure 20 depicts a detailed analysis of the transient temperature distribution trial cases of FW-GMAW and R-GMAW. Table 10 shows the peak temperatures, and the results show that a higher temperature gradient exists at the FZ due to the intense heat energy provided by the FW-GMAW, regardless of speed.

Table 10 Input parameters, measured output characteristics and calculated values of input heat

		R-GMAW									FW-GMAW								
		1	**2**	**3**	**4**	**5**	**6**	**7**	**8**	**9**	**1**	**2**	**3**	**4**	**5**	**6**	**7**	**8**	**9**
weld bead mass	*grams*	1.19	1.02	0.97	1.25	1.19	1.17	1.32	1.07	0.85	1.29	0.98	0.97	1.23	1.22	1.16	1.31	1.19	0.96
Half width of the heat source *(a)*	*mm*	3.75	3.70	3.50	3.50	3.80	3.60	3.80	3.65	3.35	4.10	3.90	3.70	4.15	3.95	3.85	4.25	4.20	3.90
Depth of the heat source (*b*)		3.30	2.82	2.70	2.98	2.56	2.50	2.80	2.70	2.38	4.90	3.80	3.30	3.20	2.80	2.70	3.52	3.38	2.98
Power density in front ellipsoid (c_f)		2.14	1.83	1.75	1.93	1.66	1.62	1.82	1.75	1.54	3.18	2.47	2.15	2.08	1.82	1.75	2.28	2.19	1.93
Power density in rear ellipsoid (c_r)		4.29	3.66	3.51	3.87	3.32	3.25	3.64	3.51	3.09	6.37	4.94	4.29	4.16	3.64	3.51	4.57	4.39	3.87
Fraction of heat deposited in front (f_f)						0.667									0.667				
Fraction of heat deposited in rear (f_r)						1.333									1.333				
Total time taken to weld (*t*)	*sec*	17.14	13.9	12.00	17.14	13.95	12.00	17.14	13.95	12.00	17.14	13.95	12.00	17.14	13.95	12.00	17.14	13.95	12.00
Input heat flux *(Front ellipsoid)*	*Watts/mm²*	2.46	0.75	0.54	1.51	0.36	0.30	1.21	0.88	0.22	9.58	4.88	2.56	2.43	0.88	0.66	5.55	4.49	2.10
Input heat flux *(Rear ellipsoid)*		53.25	50.60	51.88	65.66	59.17	61.01	86.92	87.40	80.00	38.69	49.69	54.34	64.05	62.94	63.01	82.98	84.38	89.09
Total Input heat flux		55.70	51.35	52.42	67.17	59.53	61.31	88.13	88.28	80.22	48.27	54.57	56.89	66.48	63.66	63.82	88.53	88.87	91.19
Total heat density per unit length	KJ/mm	0.41	0.25	0.19	0.41	0.27	0.22	0.49	0.38	0.24	0.49	0.37	0.24	0.52	0.36	0.32	0.54	0.44	0.33

The temperature distributions of trial cases of 4, 5, and 6 for FW-GMAW and trial case 4 for R-GMAW are considered for this paper. At the same input conditions, transient temperature contours of FW/R-GMAW process at time instants of t = 0.2s, 0.4s and time at which maximum temperature attainted are studied, details in Figure 20 (a-d). The simulation results indicated that, for the trial case 4 of R-GMAW at t1=0.2s. the transient temperature is 582°C, increased to 598°C at t2=0.4s and steady state attained at t3=0.82s which is623±3°C. i.e. the maximum steady state temperature reaches at a weld travel distance of 47.44 mm from origin. In the same way, results of trial case 4 of FW-GMAW observed that 623°C and 638°C are the transient temperatures at time instants of t1 and t2 and steady state temperature of 644°C±3 has been reached at t3=0.75s. Therefore, the steady state temperature is reached quickly in FW-GMAW, which is 7% higher that the temperature at time t1. i.e. it occurs at a weld travel distance which is 5.5% lesser than the weld travel distance at which steady state is reached, in case of R-GMAW. Similarly, trial cases 5 and 6 of FW-GMAW indicate that at time t1, the transient temperatures are 618°C and 593°C, respectively. The steady state temperatures of 632±3°C and 634±3°C have been attained at time instants of 0.38 and 0.61s, respectively.

In addition, the initial transient temperature observed is 7.18% (trial 4), 5.98% (trial 5) and 2% (trial 6) higher than that of trial 4 of R-GMAW and 4.17%, 1.44%, and 1.73% of greater steady state temperature is obtained. Therefore, results confirmed that, the initial arc and steady state temperature are higher for FW-GMAW process. The error percentage is calculated for both FW-GMAW and R-GMAW process as detailed in Table 14. In some trials, the numerical and experiment values have slight deviations which could be attributed to assumptions made in numerical model. Since the numerical results have a good agreement with the experimental results, the proposed numerical approach is applicable to welding simulation and predictions.

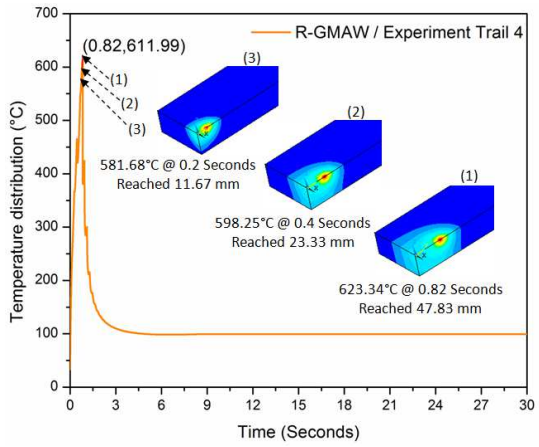

(a)Temperature zones of the transient heat source with different function of time - trial case 4 of R-GMAW

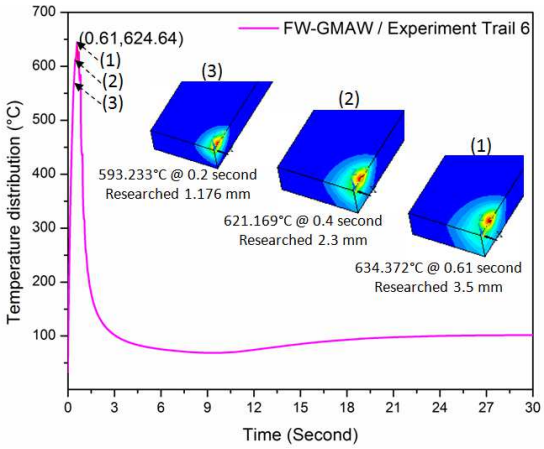

(b)Temperature zones of the transient heat source with different function of time - trial case 6 of FW-GMAW

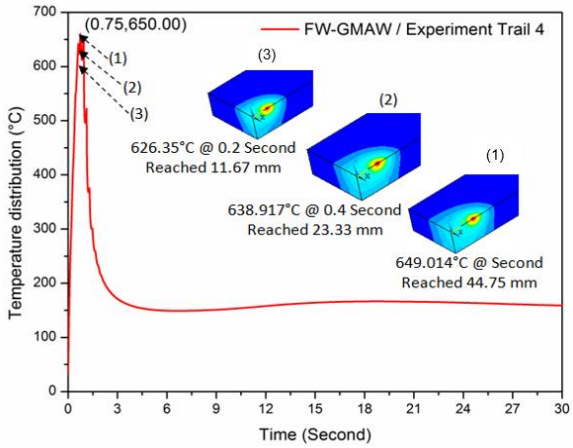

(c)Temperature zones of the transient heat source with different function of time - trial case 4 of FW-GMAW

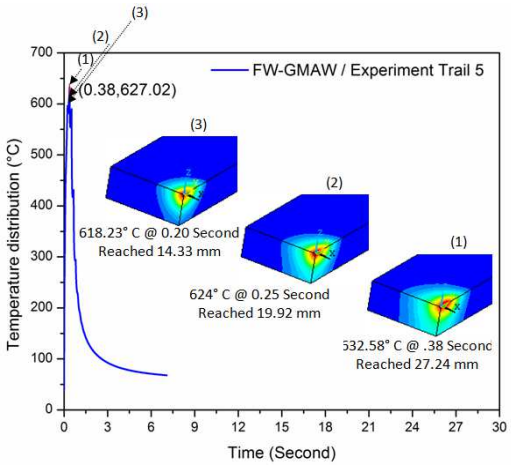

(d)Temperature zones of the transient heat source with different function of time - trial case 5 of FW-GMAW

Figure 20 The temperature contours at the top of the weld and temperature-history

5 EFFECT OF THERMO-MECHANICAL ANALYSIS

The thermal cycle during the FW-GMAW was slightly improved due to the change in geometry of the flat wire electrode. Hence, the mechanical and metallurgical behavior of the weld characteristics changed, especially the variation in grain size observed in different zones.

5.1 Significance of FW-GMAW on microhardness

"Vickers hardness tester (Zwick)" is used to determine the microhardness of all welded samples in the fusion zone (FZ) and heat affected zone (HAZ) under a constant load of 0.5 kg with step size between each indentation of 0.4 mm as per ASTME384.

The FW-GMAW weld microhardness profile shows a maximum of approximately 67.56 Hv in the very small grain size region of the FZ and 68.96 Hv due to the effect of fine grain size enlargements of the HAZ. Similarly, maximum microhardness of 60.25 Hv and 65.69 Hv in the FZ and HAZ regions respectively for R-GMAW are observed. This microhardnes approximately 1.8 times higher in FZ and 1.2 times higher for the HAZ than that of R-GMAW weld profile.

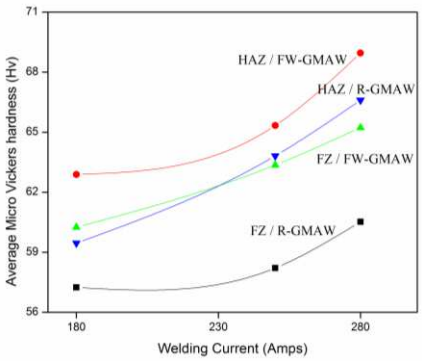

(i) Average microhardness

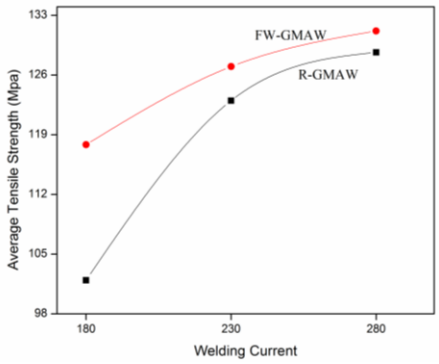

(ii) Average tensile strength

Figure 21 Observation of mechanical characteristics

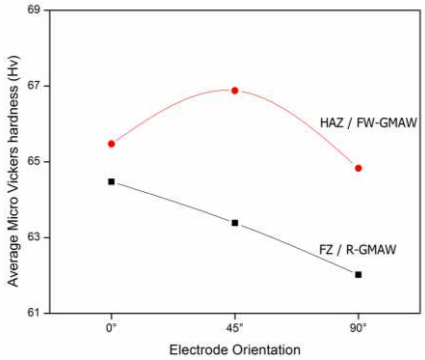

(i) Average hardness Vs Orientations

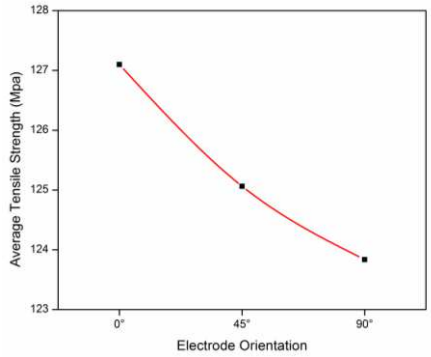

(ii) Average tensile strength Vs Orientations

Figure 22 Influence flat wire electrode orientation

Figure 20 illustrates the influence of the welding current in both the processes. An increase in the mocrohadness is reported as a result of increasing in welding current. Similarly Figure 22 indicated that the influence among the different orientations, 0° orientation of flat wire electrode has average of 5.8% and 4.8% higher micro hardness obtained in FZ with orientations of 45° and 90° in FW-GMA.

5.2 Significance of FW-GMAW on tensile strength

Tensile tests are carried out to determine the ultimate tensile strength of the weld section influenced by the FW-GMAW process. The samples are prepared according to ASTM E8M-04 guidelines.

The tensile properties such as tensile strength and percentage of elongation of all weld joints are evaluated. The average tensile values are presented in Table 11, which is for FW-GMAWeds is ranges from 111.25 MPa – 133.58 MPa. However, the tensile strength of the R-GMAW joint is 96.98 MPa – 131.29 MPa. This indicates that, the welded by FW-GMAW process is exhibited a higher tensile strength value on average 5.96% compared than that of the R-GMAW joints. Figure 20 and Figure 21 are inferred that use of the flat wire electrode always have grater has strength. Furthermore, the influences of the flat wire electrode orientation on tensile strength are calculated to be an average 1.6 % and 2.56 % of higher strength obtained in 0° orientation than 45° and 90° orientations respectively. However, the average elongation and average reduction in the cross sectional area of the FW-GMAW weld bead are 10.14% and 6.41%, respectively. Similarly, for the R-GMAW weld bead are having 9.77 % and 5.63 %, respectively. This result evidenced showed that the weld joint with FW-GMAW exhibited higher ductility values, and the improvement in ductility was approximately 3.63% compared that of the R-GMAW joints.

5.3 Significance of FW-GMAW on microstructure characterization

Grain size is one of the fundamental microstructural quantities and correlates with several properties, such as microhardness, tensile strength, elongation and fracture etc. The aim of this study is to characterize the variation in grain size in FZ and HAZ by welding of FW-GMAW and which influences the mechanical properties.

The specimens are prepared as per ASTM standard. All accepted weld samples are free from porosity. For an example, trial case 4 of the FW-GMAWed and the R-GMAWed are displayed in Figure 22.

`

The microstructure characterization of grain size variations in the FZ and HAZ was further developed by quantitative metallographic methods (40). The welded joint image is composed of an FZ, an HAZ, and a BMZ area are as shown in Figure 23.

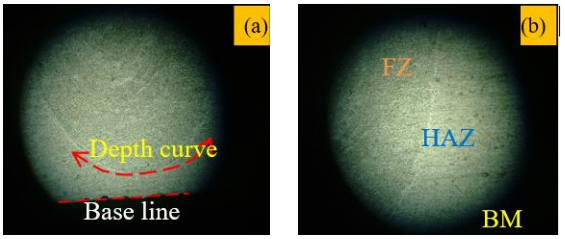

(i) A typical FW-GMAW weld joint (case 4)

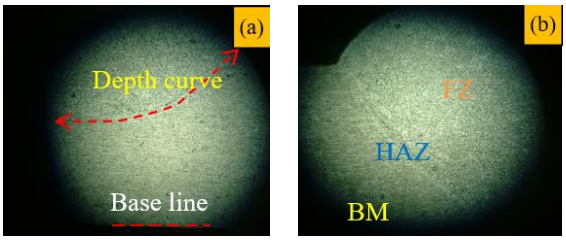

(ii) A typical R-GMAW weld joint (case 4)

Figure 23 Macrosectional view
a) deep penetration depth and b) different zone boundary

The grain distribution is visible clearly and compared with grains in both the FZ and the BM, the elongated coarse grains markedly in the HAZ and the average grain size of the FZ and HAZ are determined and tabulated in Table 11. The average areas of the penetration and HAZ. This increases by approximately 22.7 % and 12.3 % respectively. This is due to a higher heat flux is occurring during the FW-GMAW which increases the peak temperature of the molten pool and results in a wider FZ and HAZ, as shown in Figure 24 (i, iii, vii and x).

7 Results and discussion

The weld metal microstructure of any fusion welded joint is deeply influenced by the chemical composition of the filler metal and the heat input during the process. The heat input plays a leading role in controlling the microstructure and mechanical properties of GMAW welded joints Zhang et al. (41). A lower heat input results in a higher cooling rate which develops coarse grains in the weld metal and vice versa Ragu Nathan et al.(42). Maintaining optimized heat input throughout the process can to enhance the mechanical properties, as a result of grain betterment (43 & 44). The FW-GMAW process supplies an average heat input of 69.14 watts per mm^3 to the weld region compared to the R-GMAW process which supplies an average approximately 67.12 watts per mm^3. During natural cooling, mechanical action for refining microstructure process is possible. With available setup of FW-GMAW, only about 3 % of higher heat flux can be produced than that of the R-GMAW process.

Furthermore, a 4.83 % higher steady state temperature was reached during the FW-GMAW process. Due to the higher heat generation the FZ and HAZ are obtained better than the R-GMAW welded joint characteristics. In addition, the average heat density per unit length is calculated which is approximately 31 % of greater for FW-GMAW. This may be due to the influence of the flat wire electrode.

Table 11 Responses of weld bead characteristics in different experimental trial

Trial case experiments nos.	Welding parameter's			Observed and calculated value of weld bead characteristics															
				FW-GMAW								R-GMAW*							
				Average Micro Vickers hardness (Hv)		Tensile Strength property				Calculated grain size (µm)		Average Micro Vickers hardness (Hv)		Tensile Strength property				Calculated grain size (µm)	
	Welding Current (I)	Welding Speed (WS) mm/min	Flat wire Electrode Orientation (θ)	FZ	HAZ	Value (MPa)	Elongation (%)	Reduction in cross sectional area (%)	Failure Location	FZ	HAZ	FZ	HAZ	Value (MPa)	Elongation (%)	Reduction in cross sectional area (%)	Failure Location	FZ	HAZ
1	180	350	0°	61.82	63.56	125.21	09.52	5.38	FZ	10.4	11.9	58.23	61.25	110.25	09.25	5.21	HFZ	09.4	10.5
2	180	430	45°	59.35	63.25	117.05	08.98	4.36	HAZ#	09.1	10.1	57.12	60.25	098.61	08.95	4.85	HAZ	08.7	09.9
3	180	500	90°	57.21	61.86	111.25	08.35	4.21	HAZ	08.5	09.9	56.38	59.25	096.98	08.59	4.45	FZ	07.3	09.2
4	230	350	45°	64.46	68.63	128.25	09.86	5.75	HAZ	10.9	12.2	58.96	64.58	125.22	10.45	7.35	FZ	09.5	10.6
5	230	430	90°	61.29	63.48	126.68	09.25	5.35	HAZ	09.5	10.2	56.89	63.25	123.54	09.89	5.89	HAZ	08.5	09.8
6	230	500	0°	65.71	63.90	126.04	09.85	6.11	Near FZ	09.2	09.8	55.78	62.25	120.25	09.35	6.20	FZ	07.9	09.2
7	280	350	90°	67.56	69.15	133.58	11.72	8.21	HAZ	11.8	13.2	62.21	66.15	131.29	12.30	8.21	HAZ	10.5	11.5
8	280	430	0°	65.89	68.96	130.05	10.56	7.85	HMZ	10.2	11.5	60.25	65.69	128.14	11.65	7.87	FZ	09.6	10.4
9	280	500	45°	66.35	68.76	129.89	09.85	6.15	HAZ	09.4	10.1	59.12	63.85	126.57	10.83	7.69	HAZ	08.3	10.1

Electrode orientation is not applicable for R-GMAW process* ***FZ* *– Fusion zone* ***HAZ*** *– Heat affected zone* ***BMZ*** *– Base metal zone* *# Boundary of BMZ and HAZ*

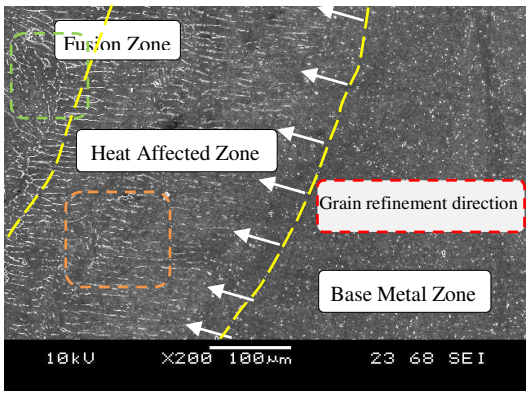

(i) Typical zones of R-GMAW (trial case 4)

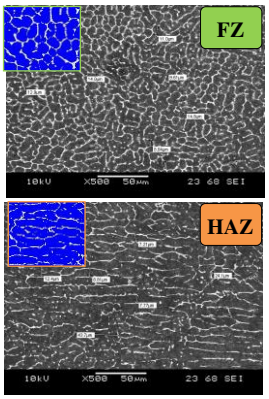

(ii) Grain size measurement from SEM image

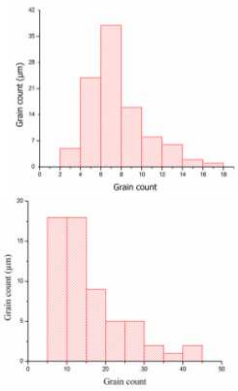

(iii) Grain size distribution histogram

Mean : 7.5 µm
SD : 2.5 µm

Avg. grain size from SEM image
9.5 µm

Mean : 12.5 µm
SD : 8.9 µm

Avg. grain size from SEM image
10.6 µm

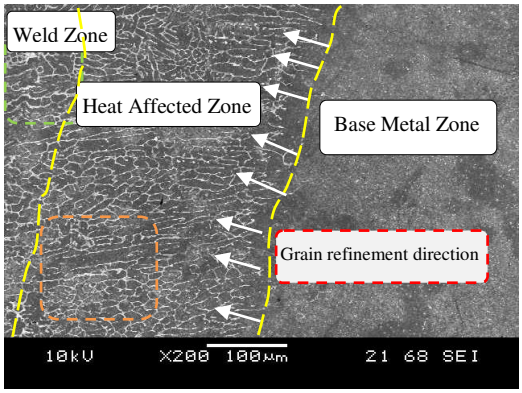

(iv) Typical zones of 90˚ electrode orientation of FW-GMAW (trial case 5)

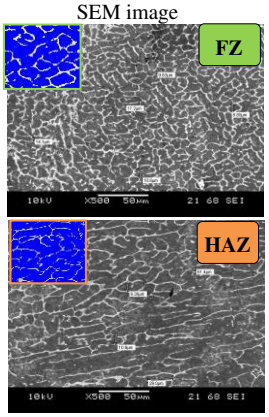

(v) Grain size measurement from SEM image

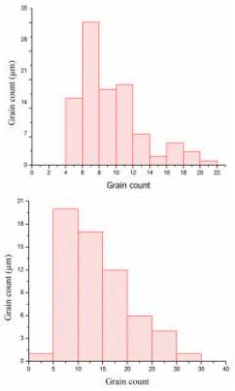

(vi) Grain size distribution histogram

Mean : 9.1µm
SD : 3.5 µm

Avg. grain size from SEM image
9.5 µm

Mean : 10.2 µm
SD : 6.3 µm

Avg. grain size from SEM image
9.7 µm

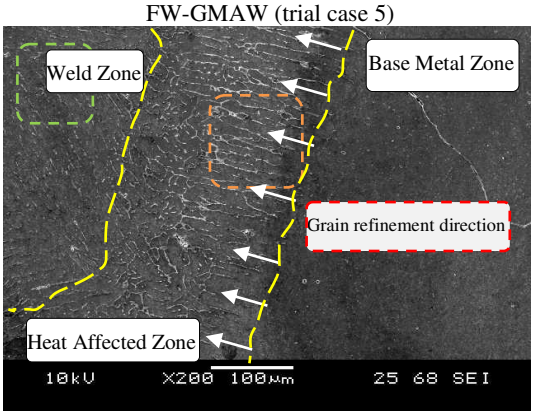

(vii) Typical zones of 45˚ electrode orientation of FW-GMAW (trial case 4)

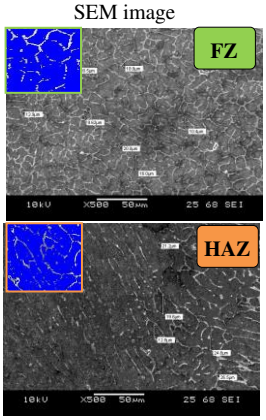

(viii) Grain size measurement from SEM image

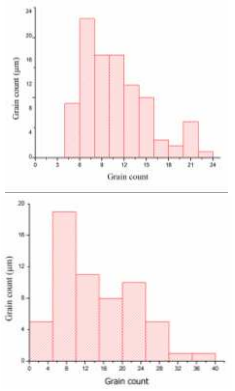

(ix) Grain size distribution histogram

Mean : 11.2µm
SD : 4.2 m

Avg. grain size from SEM image
10.9 µm

Mean : 11.9 µm
SD : 7.9µm

Avg. grain size from SEM image
12.8 µm

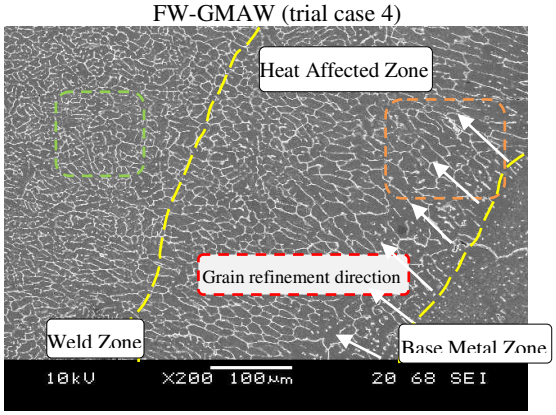

(x) Typical zones of 0º electrode orientation of FW-GMAW (trial case 6)

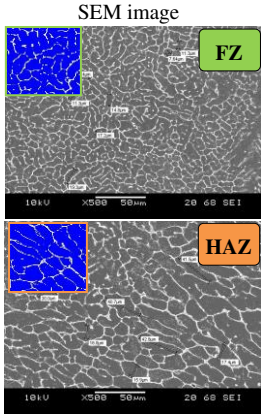

(xi) Grain size measurement from SEM image

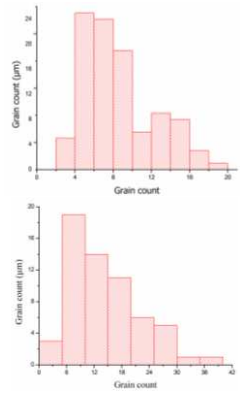

(xii) Grain size distribution histogram

Mean : 8.5µm
SD : 3.6 µm

Avg. grain size from SEM image
9.5 µm

Mean : 14µm
SD : 7.9µm

Avg. grain size from SEM image
12.2 µm

Figure 24 Different zones and the grain size distribution of FW-GMAW and R-GMAW

`

An increase in heat flux provides more a driving force for grain boundary migration and then speeds the growth of the grains (45). A small grain enlargement was placed in the FZ and HAZ, and the direction of grain elongation toward the FZ as shown in Figure 25. The average grain size is calculated for all the trial case experiments, details are provided in Table 11. There are no major improvements in grain size in FW-GMAW's FZ and HAZ. The average of grain size (including FZ and AZ) is calculated ranges from 9.2 - 13.2 µm (heat flux range of range of 0.24 - 0.54 kJ/mm) for FW-GMAW whereas 8.2 - 11 µm (heat flux range of 0.19 - 0.49 kJ/mm) for R-GMAW which indicated that the overall grain size increased about 9 % for FW-GAMW. However, influence of flat wire electrode orientation revealed that approximately 5 % grain size is increased for 0˚ orientation than that of 45˚ and 90˚ orientations. In most of the FZ fine equiaxed grains become the major solidification structure, similar to HZA having cellular in structure, details in Figure 24 (ii, v, viii & xi). Uniform heat flow transfer occurs during the FW-GMAW and R-GMAW processes, which is evident in the Figure 25 (i & ii).

Furthermore, the trial cases of 4, 5 and 6 for FW-GMAW and trial case 4 for R-GMAW are considered for comparison. Figure 24 displays the SEM images of the FZ and HAZ surfaces and corresponding Gaussian fitting of the grain size statistical data are shown in Figure 24 (iii, vi, ix & xii). The average grain size in the R-GMAW is about 9.5 µm (FZ) and 10.6 µm (HAZ). For the FW-GMAW, the average grains increase to about 10.9 µm (FZ) and 12.8 µm (HAZ), 9.5 µm (FZ) and 9.7 µm (HAZ) and 9.5 µm and 12.2 µm (HAZ) for 45˚, 90˚ and 0˚ respectively. The increased grain size decreases the grain boundary width, decreasing the probability of crack growth or poor bonding and minimizing residual stresses in the weld Zhang et al. (41). However, the grain count is measured for all samples of FZ and HAZ using Image j software. The histogram inferred that, there is a small improvement in grain count of FW-GMAW. Even increased grain size of FW-GMAW is not affecting the corresponding mechanical properties, rather microhardness and tensile properties has improved. Therefore, optimized weld parameters will help in obtaining defect free welds and grain size and boundary have no significant role on the mechanical properties of weld joints at room temperature Manwatkar et al. (46) and Gupta et al. (47)

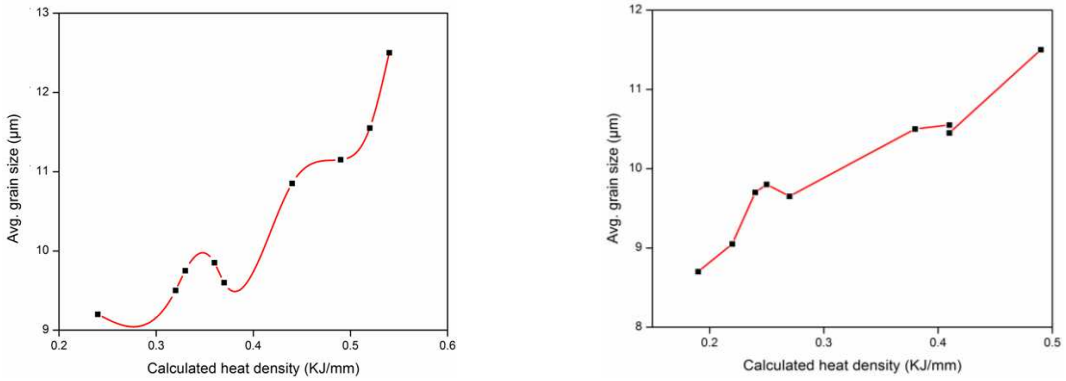

(i) For FW-GMAW **(ii)** For R-GMAW

Figure 25 Graph for grain size versus heat flux

8 CONCLUSION

The effects of flat wire electrode for improving the dimensional quality and the mechanical properties of the weld in GMAW process is successfully investigated in this paper. The main conclusions are drawn

The conventional GMAW process has been tailored to form flat wire electrode by the development of Modified Wire Feeder (MWF) mechanism, Support Wire Feeder (SWF) system and new straight head welding torch.

The conventional 1.2 mm diameter of wire electrode made of Er4043 is formed into flat wire electrode, which is very closer to cross-sectional area of regular or cylindrical wire electrode is preferred which have 27.5 % of higher perimeter than the regular wire electrode

The electric and magnetic field were noted to be 1.9 and 1.23 times that of cylindrical wire electrode. The test results inferred that, an increase in the perimeter of the flat wire electrode will increase the electric and magnetic fields.

The butt joint is performed and the macrostructure examination revealed that the D/W ratio of FW-GMAW has improved by 7.73%. However, ~ 0.266 mm and ~ 0.766 mm of higher weld bead width is noted in 45º orientation than 0º and 90º orientations of FW-GMAW process. Similarly ~ 0.166 mm and ~ 0.22 mm of higher penetration depth obtained in 0º orientation than 45º and 90º orientations of FW-GMAW process.

The error percentages have been determined and the maximum error % of the predicted values for the weld bead width and penetration is 1.4 % and 2.8 % respectively.

Transient temperature distribution at the top surface of weld bead zone has been measured inline during the process, which is 7.31% of higher temperature distribution for FW-GMAW than that of R-GMAW process.

FZ and HAZ are affected by FW-GMAW and it became widened with the increase of heat flux, also the grain size of FZ and HAZ is found to be fine equiaxed grains on FZ and cellular in structure established in the lower region of weld metal (HAZ). There is no change in grain morphology as heat flux varied.

As increase in heat flux results in increases in width and depth of FZ and HAZ and also grain size of the FZ and HAZ increased for FW-GMAW. Over all grain size is amplified 9 % (includes FZ and HAZ) in FW-GMAW than that of R-GMAW.

All FW-GMAW weld specimens exhibit improved mechanical characteristics as compared to R-GMAW values, with average microhardness and tensile properties of 7.2% and 5.96% higher, respectively.

Therefore, FW-GMAW is better alternate to enhance the weld bead characteristics.

REFERENCE

1) Karuthapandi, S., M. Ramu, and P. R. Thyla. 2017. "Effects of the Use of a Flat Wire Electrode in Gas Metal Arc Welding and Fuzzy Logic Model for the Prediction of Weldment Shape Profile." Journal of Mechanical Science and Technology 31(5).

2) Kim, Il Soo, Ji Hye Lee, Javad Malekani, and Prasad K. D. V. Yarlagadda. 2014. "Prediction of GMA Welding Characteristic Parameter by Artificial Neural Network System." Advanced Materials Research 1061–1062:481–91.

3) Praveen Kumar Y and Vijayakumar. 2012. "Taguchi's Robust Design of Parameters of Shielded Metal Arc Welding to Weld Commercial Pipes." Pp. 11–13 in International Conference on Challenges and Opportunities in Mechanical Engineering, Industrial Engineering and Management Studies (ICCOMIM - 2012).

4) Kim I S, Lee, J H, Malekani J, Yarlagadda P. K. D. V. 2015. "Prediction of GMA Welding Characteristic Parameter by Artificial Neural Network System." Advanced Materials Research 481–91.

5) Narang, H. K., M. M. Mahapatra, and P. K. Jha. 2012. "Comparative Studies between Statistical and Soft Computing Technique to Predict the Weldment Characteristics of SAW Processes." 2(1):1–7.

6) Chan, Kr, Nigel Scotchmer, Jc Bohr, Ibraheem Khan, M. L. Kuntz, and Norman Y. Zhou. 2006. "Effect of Electrode Geometry on Resistance Spot Welding of AHSS." Sheet Metal Welding Conference XII 780:1–12.

7) Talabi, S. I., O. B. Owolabi, J. A. Adebisi, and T. Yahaya. 2014. "Effect of Welding Variables on Mechanical Properties of Low Carbon Steel Welded Joint." Advances in Production Engineering And Management 9(4):181–86.

8) Tsai, M. C., and Sindo Kou. 1990. "Heat Transfer and Fluid Flow in Welding Arcs Produced by Sharpened and Flat Electrodes." *International Journal of Heat and Mass Transfer* 33(10):2089–98.

9) Fukuhisa, U. Masao and M. 1982. "Mathematical Modelling of Heat Transfer of Welding Arc (Part 1)." Transactions of JWRI 11(1).

10) Li, K. H., and Y. M. Zhang. 2008. "Consumable Double-Electrode GMAW Part II: Monitoring, Modeling, and Control." Welding Journal (Miami, Fla) 87(2).

11) Shi, Y., X. Liu, Y. Zhang, and M. Johnson. 2008. "Analysis of Metal Transfer and Correlated Influences in Dual-Bypass GMAW of Aluminum." Welding Journal (Miami, Fla) 87(9):229–36.

12) Fang, Chen fu, Xiao hui Meng, Qing xian Hu, Feng jiang Wang, He Ren, Hai song Wang, Yu Guo, and Ming Mao. 2012. "TANDEM and GMAW Twin Wire Welding of Q690 Steel Used in Hydraulic Support." Journal of Iron and Steel Research International 19(5):79–85.

13) Karuthapandi, S., and R. Murugan. 2017. "An Experimental Investigation of Flat Wire Electrodes and Their Weld Bead Quality in the FCAW Process." High Temperature Material Processes 21(1).

14) Sripriyan, K., and M. Ramu. 2016. "Analysis of Weld Bead Characteristics on GMAW by Changing Wire Electrode Geometry." *Journal of Achievements in Materials and Manufacturing Engineering* 78(2):49–58.

15) Nezamdost, M. R. Nekouie Esfahani, S. H. Hashemi, and S. A. Mirbozorg. 2016. "I, Investigation of Temperature and Residual Stresses Field of Submerged Arc Welding by Finite Element Method and Experiments." Int J Adv Manuf Technol 87:615–624.

16) Rosenthal, D. 1946. "The Theory of Moving Sources of Heat and Its Application to Metal Treatments." Transactions ASME 43:849–66.

17) N, Rykalin N. 1951. *Rasczioty Tieplowych Processow Pri Svarke, Moskwa, Masgiz.*

18) Eagar, T. W., Oreper, G., and Szekely. 1983. J., Weld. J., 62: 307s.

19) K.S. Bo, H. S. Cho. 1990. "Transient Temperature Distribution in Arc Welding of Finite Thickness Plates." Proc. Inst. Mech. Eng. 204(B3):175–183.

20) Nguyen n. T, Y.-W. Mai , simpson S, and ohta A. 2004. "Analytical Approximate Solution for Double Ellipsoidal Heat Source in Finite Thick Plate." Welding Journal 3:82–93.

21) Goldak J, Chakravarti A, Bibby M. 1985. "A Double Ellipsoidal Finite Element Model for Welding Heat Source." II W Doc.

22) Aniruddha Ghosh, Himadri Chattopadhyay. 2013. "Mathematical Modeling of Moving Heat Source Shape for Submerged Arc Welding Process." Int J Adv Manuf Technol 69:2691–2701.

23) Karuthapandi, S., R. Murugan, and P. K. Palani. 2016. "Study and Analysis of the Macrostructure Characteristics in FCAW with the Use of a Flat Wire Electrode and by Optimizing the Process Parameter Using the Taguchi Method and Regression Analysis." High Temperature Material Processes 20(3). doi: 10.1615/HighTempMatProc.2016017429.

24) Kazeem K. Adewole. 2012. "Simulation of the Wire Reverse Bending Test." Journal of Civil Engineering and Construction Technology 3(3):116–26.

25) Lancaster, J. F. 1987. "The Physics of Fusion Welding Part 2: Mass Transfer and Heat Flow." IEE Proceedings B: Electric Power Applications 134(6):297–316.

26) H. GuoMing, Z. Jian and L. JianQang. 2007. "Dynamic Simulation of the Temperature Field of Stainless Steel Laser Welding." Materials & Design 28(1):240–45.

27) Das J E R and Kumanan S. 2007. "ANFIS for Prediction of Weld Bead Width in a Submerged Arc Welding Process." *Journal of Scientific & Industrial Research* 5(66):335-338.

28) Gery, D., H. Long, and P. Maropoulos. 2005. "Effects of Welding

Speed, Energy Input and Heat Source Distribution on Temperature Variations in Butt Joint Welding." Journal of Materials Processing Technology 167(2–3):393–401.

29) Frappier, R., A. Benoit, P. Paillard, T. Baudin, R. Le Gall, and T. Dupuy. 2014. "Quantitative Infrared Analysis of Welding Processes: Temperature Measurement during RSW and CMT-MIG Welding." *Science and Technology of Welding and Joining* 19(1):38–43.

30) M.C. Zondi, Y. Tekane, E. Magidimisha, E. Wium, A. Gopal, C. Bemont. 2017. "Characterisation of Submerged Arc Welding Process Using Infrared Imaging Technique,." R & D Journal of the South African Institution of Mechanical Engineering 33(66–74).

31) Rana, K. P. S. 2011. "Fuzzy Control of an Electrodynamic Shaker for Automotive and Aerospace Vibration Testing." Expert Systems with Applications 38(9):11335–46.

32) Zadeh, L. A. 1965. "Fuzzy Set." Pp. 338–53 in information and control.

33) Bandler W, Kohout L. 1988. "Special Properties, Closures and Interiors of Crisp and Fuzzy Relations." Fuzzy Sets and Systems 26(3):317–32.

34) Nirsanametla YADAIAH and Swarup BAG. 2012. "Effect of Heat Source Parameters in Thermal and Mechanical Analysis of Linear GTA Welding Process." ISIJ International 52(11):2069–75.

35) Darmadi, Djarot B., Anh Kiet Tieu, and John Norrish. 2012. "A Validated Thermal Model of Bead-on-Plate Welding." Heat and Mass Transfer/Waerme- Und Stoffuebertragung 48(7):1219–30.

36) Sripriyan, K., M. Ramu, P. R. Thyla, and K. Anantharuban. 2021. "Weld Bead Characterization of Flat Wire Electrode in Gmaw Process Part II : A Numerical Study." 35(5):1–8.

37) Bai-Qiao Chen, and C. Guedes Soares. 2016. "Effect of Welding Sequence on Temperature Distribution, Distortions, and Residual Stress on Stiffened Plates." Int J Adv Manuf Technol 86:3145–3156.

38) Kong, F., Lin, D., Yang, S., Kovacevic, R. 2008. "Numerical Analysis of a Hybrid Laser–Arc Welding Process by Using 3D Nonlinear Finite Element Model." in . In: The Proceeding of 47th Conference of Metallurgical (COM2008), Winnipeg, Manitoba, Canada.

39) Fukuhisa, U. Masao and M. 1982. "Mathematical Modelling of Heat Transfer of Welding Arc (Part 1)." Transactions of JWRI 11(1).

40) Kupczyk, J. 2006. "Application of Significance Tests in Quantitative Metallographic Analysis of a C-Mn-B Steel." Materials Characterization 57(3):171–75.

41) Zhang, Ying qiao, Han qian ZHANG, Jin fu LI, and Wei ming LIU. 2009. "Effect of Heat Input on Microstructure and Toughness of Coarse Grain Heat Affected Zone in Nb Microalloyed HSLA Steels." Journal of Iron and Steel Research International 16(5):73–80.

42) Ragu Nathan, S., V. Balasubramanian, S. Malarvizhi, and A. G. Rao. 2015. "Effect of Welding Processes on Mechanical and Microstructural Characteristics of High Strength Low Alloy Naval Grade Steel Joints." Defence Technology 11(3):308–17.

43) Yayla, P., E. Kaluc, and K. Ural. 2007. "Effects of Welding Processes on the Mechanical Properties of HY 80 Steel Weldments." Materials and Design 28(6):1898–1906.

44) Sripriyan K, Prashanth M, Ramu M, Thyla P. R. 2017. "Analysis of Molten Pool Characteristics on Hybrid GMAW Process." Asian Journal of Research in Social Sciences and Humanities 7(10):142–54.

45) Min, Dong, Jun Shen, Shiqiang Lai, and Jie Chen. 2009. "Effect of Heat Input on the Microstructure and Mechanical Properties of Tungsten Inert Gas Arc Butt-Welded AZ61 Magnesium Alloy Plates." Materials Characterization 60(12):1583–90.

46) Manwatkar, Sushant K., M. Sunil, Antony Prabhu, S. V. S. Narayana Murty, Reji Joseph, and P. Ramesh Narayanan. 2019. "Effect of Grain Size on the Mechanical Properties of Aluminum Alloy AA2219 Parent and Weldments at Ambient and Cryogenic Temperature." Transactions of the Indian Institute of Metals 72(6):1515–19.

47) Gupta, R. K., and S. V. S. Naraya. Murty. 2006. "Analysis of Crack in Aluminium Alloy AA2219 Weldment." Engineering Failure Analysis 13(8):1370–75.